.

WHERE STARS FORM: INSIDE-OUT GROWTH AND COHERENT STAR FORMATION FROM HST Hα MAPS OF 2676 GALAXIES ACROSS THE MAIN SEQUENCE AT Z ∼ 1

Erica June Nelson[1], Pieter G. van Dokkum[1], Natascha M. Förster Schreiber[2], Marijn Franx[3], Gabriel B. Brammer[4], Ivelina G. Momcheva[1], Stijn Wuyts[2], Katherine E. Whitaker[5], Rosalind E. Skelton[6], Mattia Fumagalli[3], Mariska Kriek[7], Ivo Labbé[3], Joel Leja[1], Hans-Walter Rix[8], Linda J. Tacconi[2], Arjen van der Wel[8], Frank C. van den Bosch[1], Pascal A. Oesch[1], Claire Dickey[1], Johannes Ulf Lange[1]

Draft version July 16, 2015

ABSTRACT

We present Hα maps at 1 kpc spatial resolution for star-forming galaxies at $z \sim 1$, made possible by the WFC3 grism on HST. Employing this capability over all five 3D-HST/CANDELS fields provides a sample of 2676 galaxies enabling a division into subsamples based on stellar mass and star formation rate. By creating deep stacked Hα images, we reach surface brightness limits of $1 \times 10^{-18}\,\mathrm{erg\,s^{-1}\,cm^{-2}\,arcsec^{-2}}$, allowing us to map the distribution of ionized gas out to greater than 10 kpc for typical L* galaxies at this epoch. We find that the spatial extent of the Hα distribution increases with stellar mass as $r_{\mathrm{H\alpha}} = 1.5(M_*/10^{10}M_\odot)^{0.23}$ kpc. Furthermore, the Hα emission is more extended than the stellar continuum emission, consistent with inside-out assembly of galactic disks. This effect, however, is mass dependent with $r_{\mathrm{H\alpha}}/r_* = 1.1(M_*/10^{10}M_\odot)^{0.054}$, such that at low masses $r_{\mathrm{H\alpha}} \sim r_*$. We map the Hα distribution as a function of SFR(IR+UV) and find evidence for 'coherent star formation' across the SFR-M* plane: above the main sequence, Hα is enhanced at all radii; below the main sequence, Hα is depressed at all radii. This suggests that at all masses the physical processes driving the enhancement or suppression of star formation act throughout the disks of galaxies. It also confirms that the scatter in the star forming main sequence is real and caused by variations in the star formation rate at fixed mass. At high masses ($10^{10.5} < M_*/M_\odot < 10^{11}$), above the main sequence, Hα is particularly enhanced in the center, indicating that gas is being funneled to the central regions of these galaxies to build bulges and/or supermassive black holes. Below the main sequence, the star forming disks are more compact and a strong central dip in the EW(Hα), and the inferred specific star formation rate, appears. Importantly though, across the entirety of the SFR-M* plane we probe, the absolute star formation rate as traced by Hα is always centrally peaked, even in galaxies below the main sequence.

Subject headings: galaxies: evolution — galaxies: formation — galaxies: high-redshift — galaxies: structure — galaxies: star formation

1. INTRODUCTION

The structural formation history of galaxies is written by the spatial distribution of their star formation through cosmic time. Recently, the combination of empirical modeling and observations of the scaling relation between stellar mass and star formation rate has enabled us to constrain the build up of stellar mass in galaxies over a large fraction of cosmic time (Yang et al. 2012; Leja et al. 2013; Behroozi et al. 2013; Moster, Naab, & White 2013; Lu et al. 2014; Whitaker et al. 2014). The dawn of Wide Field Camera 3 (WFC3) on the Hubble Space Telescope (HST) has enabled us to map the structural growth of this stellar mass content of galaxies at high fidelity over a large fraction of the history of the universe (e.g. Wuyts et al. 2011a, 2012; van der Wel et al.

2012; van der Wel et al. 2014a, 2014b; Bruce et al. 2014; Boada et al. 2015; Peth et al. 2015). It has become clear that the physical sizes of galaxies increase with cosmic time as the universe expands (Giavalisco, Steidel, & Macchetto 1996; Ferguson et al. 2004; Oesch et al. 2010; Mosleh et al. 2012; Trujillo et al. 2006; Franx et al. 2008; Williams et al. 2010; Toft et al. 2007; Buitrago et al. 2008; Kriek et al. 2009; van der Wel et al. 2014a). For star forming galaxies, with increasing stellar mass, the disk scale length increases as does the prominence of the bulge (e.g. Shen et al. 2003; Lang et al. 2014). The picture that has emerged from these studies is that most galaxies form their stars in disks growing inside out (Wuyts et al. 2011a, 2013; van der Wel et al. 2014b; Abramson et al. 2014).

In the canonical paradigm, inside-out growth is a consequence of the dark mater halo properties of the galaxies. Galaxies are thought to accrete their gas from the cosmic web at a rate throttled by the mass of their dark matter halo (e.g. White & Rees 1978; Dekel et al. 2013). The gas cools onto the disk of the galaxy and forms stars with a radial distribution set by the angular momentum distribution of the halo (Fall & Efstathiou 1980; Dalcanton, Spergel, & Summers 1997; van den Bosch 2001). As the scale factor of the universe increases, so does the spatial extent of the gas (Mo, Mao, & White 1998); galaxies were smaller in the past and grow larger with time, building up from the inside-out. However, the actual formation of galaxies in a cosmological context is

[1] Astronomy Department, Yale University, New Haven, CT 06511, USA
[2] Max-Planck-Institut für extraterrestrische Physik, Giessenbachstrasse, D-85748 Garching, Germany
[3] Leiden Observatory, Leiden University, Leiden, The Netherlands
[4] Space Telescope Science Institute, 3700 San Martin Drive, Baltimore, MD 21218, USA
[5] Astrophysics Science Division, Goddard Space Flight Center, Greenbelt, MD 20771, USA
[6] South African Astronomical Observatory, P.O. Box 9, Observatory, 7935, South Africa
[7] Department of Astronomy, University of California, Berkeley, CA 94720, USA
[8] Max Planck Institute for Astronomy (MPIA), Königstuhl 17, 69117, Heidelberg, Germany

more complex (e.g., van den Bosch 2001; Hummels & Bryan 2012). Recently, significant progress has been made by the creation of realistic disk galaxies in hydrodynamical simulations (Governato et al. 2010; Agertz, Teyssier, & Moore 2011; Guedes et al. 2011; Brooks et al. 2011; Stinson et al. 2013; Aumer et al. 2013; Marinacci, Pakmor, & Springel 2013) and combining theory and observations in a self-consistent framework (Keres et al. 2009; Dekel & Birnboim 2006; Dekel et al. 2009b; Genzel et al. 2008, 2011; Förster Schreiber et al. 2009, 2011a; Wuyts et al. 2011b, 2011a). How gas is accreted on to galaxies (e.g. Brooks et al. 2009; Sales et al. 2012) and feedback (e.g. Keres et al. 2005; Sales et al. 2010; Übler et al. 2014; Nelson et al. 2015; Genel et al. 2015) have been shown to be essential ingredients. However, precisely what physical processes drive the sizes, morphologies, and evolution of disk galaxies is still a matter of much debate (see, e.g., Dutton & van den Bosch 2012; Scannapieco et al. 2012).

Furthermore, the evidence for this picture is indirect: we do not actually observe star formation building up different parts of these galaxies. Instead, we infer it based on empirically linking galaxies across cosmic time and tracking radial changes in stellar surface densities and structural parameters (van Dokkum et al. 2010; Wuyts et al. 2011a; van Dokkum et al. 2013; Patel et al. 2013; van der Wel et al. 2014a; Brennan et al. 2015; Papovich et al. 2015). However, this method has uncertainties due to scatter in stellar mass growth rates and merging (e.g. Leja et al. 2013; Behroozi et al. 2013). Furthermore, migration and secular evolution may have changed the orbits of stars after their formation such that they no longer live in their birthplaces (e.g., Roškar et al. 2008).

The missing piece is a direct measurement of the spatial distribution of star formation within galaxies. This is crucial to understanding the integrated relations of galaxy growth between SFR and M_*. The spatial distribution of star formation yields insights into what processes drive the star formation activity, evolution of stellar mass, and the relation between them. It helps to disentangle the role of gas accretion, mergers, and secular evolution on the assembly history of galaxies. Furthermore, this provides a test of inside-out growth which appears to be a crucial feature of galaxy assembly history.

What is required is high spatial resolution maps of star formation and stellar continuum emission for large samples of galaxies while they were actively forming their disks. The Hα flux scales with the quantity of ionizing photons produced by hot young stars, serving as an excellent probe of the sites of ongoing star formation activity (Kennicutt 1998). A number of large surveys have used Hα to probe the growth of evolving galaxies, including recently: HiZELS (Geach et al. 2008; Sobral et al. 2009), WISP (Atek et al. 2010), MASSIV (Contini et al. 2012), SINS/zC-SINF (Förster Schreiber et al. 2006, 2009), KROSS, Stott et al. (2014), and KMOS^{3D} (Wisnioski et al. 2015). Broadband rest-frame optical imaging provides information on the stellar component. The spatial distribution of this stellar light contains a record of past dynamical processes and the history of star formation. The comparison of the spatial distribution of ionized gas and stellar continuum emission thus provides an essential lever arm for constraining the structural assembly of galaxies. This potent combination shed light on the turbulent early phase of massive galaxy growth at $z \sim 2$ (Förster Schreiber et al. 2011a; Genzel et al. 2014a; Tacchella et al. 2015b, 2015a), and the spatially-resolved star-forming sequence (Wuyts et al. 2013). To apply this same methodology to a global structural analysis

requires high spatial resolution spectroscopic measurements for a large sample of galaxies. An ideal dataset would also contain broadband optical imaging with the same high spatial resolution to allow for robust comparison of the spatial distribution of ionized gas and stellar continuum emission.

This has now become possible with the WFC3 grism capability on HST. The combination of WFC3's high spatial resolution and the grism's low spectral resolution provides spatially resolved spectroscopy. Because this spectrograph is slitless, it provides a spectrum for every object in its field of view. This means that for every object its field of view and wavelength coverage, the grism can be used to create a high spatial resolution emission line map. The 3D-HST legacy program utilizes this powerful feature for a 248 orbit NIR imaging and grism spectroscopic survey over the five CANDELS fields (van Dokkum et al. 2011; Brammer et al. 2012a, Momcheva et al. in prep). In this paper, we use data from the 3D-HST survey to map the spatial distribution of Hα emission (a tracer of star formation) and H_{F140W} stellar continuum emission (rest-frame 7000Å, a proxy for the stellar mass) for a sample of 2676 galaxies at 0.7<z<1.5. The Hα and stellar continuum are resolved on scales of 0.13". This represents the largest survey to date of the spatially resolved properties of the Hα distribution in galaxies at any epoch. This spatial resolution, corresponding to $\sim 1\,$kpc, is necessary for structural analysis and only possible from the ground with adaptive optics assisted observations on 10m class telescopes. This dataset hence provides a link between the high spatial resolution imaging datasets of large samples of galaxies with HST and high spatial resolution emission line maps of necessarily small samples with AO on large ground-based telescopes. This study complements the large MOSDEF (Kriek et al. 2015) and KMOS^{3D} (Wisnioski et al. 2015) spectroscopic surveys by providing higher spatial resolution emission line measurements.

We present the average surface brightness profiles of Hα and stellar continuum emission in galaxies during the epoch $0.7 < z < 1.5$. We analyze Hα maps for 2676 galaxies from the 3D-HST survey to trace the spatial distribution of star formation. Our sample cuts a large swath through the SFR-M_* plane covering two orders of magnitude in stellar mass $10^9 < M_* < 10^{11}$ and star formation rate $1 < SFR < 400\,\mathrm{M_\odot/yr}$ and encompassing the star forming "main sequence" (MS). Wuyts et al. (2012) showed that the bright, visually striking clumps of star formation which appear to be common in high redshift galaxies are short-lived and contribute little to the integrated SFR of a galaxy. Here, we average over these short-lived clumps by stacking Hα maps. Stacking thousands of HST orbits provides deep average Hα images that allow us to trace the Hα distribution down to a surface brightness limit of $1 \times 10^{-18}\,\mathrm{erg\,s^{-1}\,cm^{-2}\,arcsec^{-2}}$ in our deepest stacks, an order of magnitude fainter than previous studies in the high redshift universe. This enables us to measure the star formation surface density down to a limit of is $4 \times 10^{-4}\,\mathrm{M_\odot\,yr^{-1}\,kpc^{-2}}$. With these deep stacked images, the primary goals of this study are to derive the average surface brightness profile and effective radius of Hα as a function of mass and star formation rate to provide insight into where star formation occurs in galaxies at this epoch.
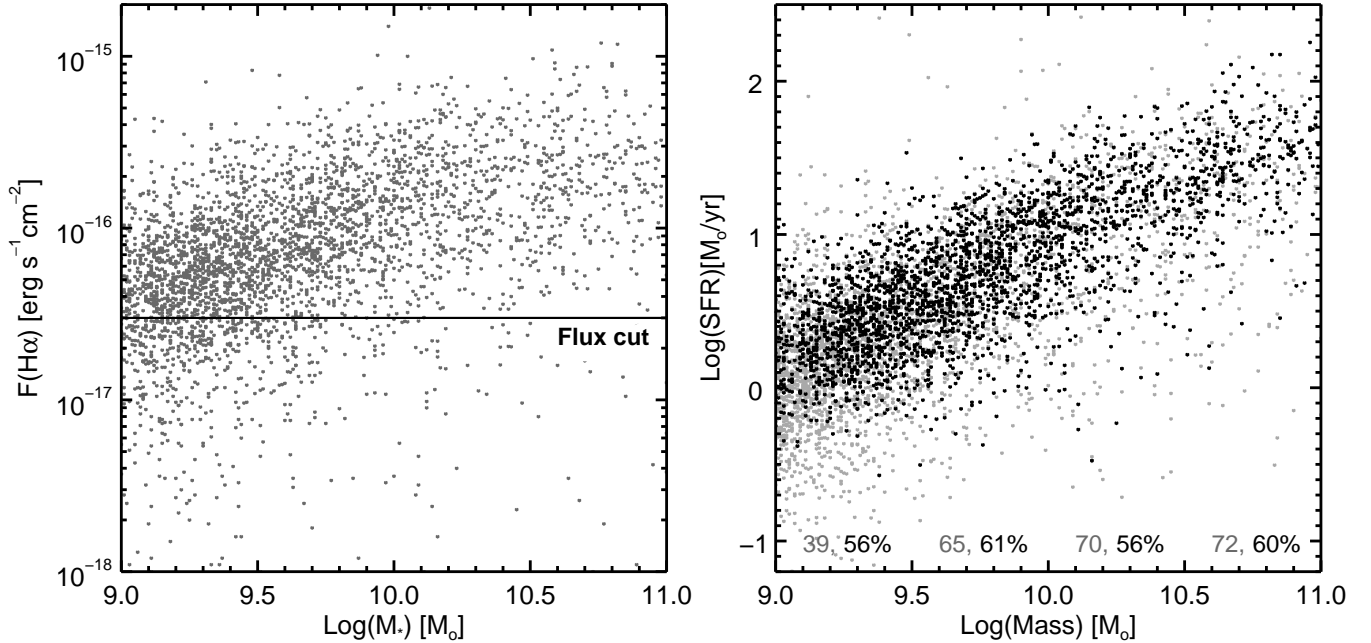
FIG. 1.— Sample selection. The left panel shows the location of our flux cut with respect to the locus of galaxies in the F(Hα)-M$_*$ plane. The right panel shows the distribution of our sample in the SFR-M$_*$ plane. The SFRs come from the UV+IR. The parent sample is shown in gray; selected galaxies are shown in black. The fraction of the total parent sample above the Hα flux limit and extraction magnitude limit are listed at the bottom in gray. As expected, we are significantly less complete at low masses and star formation rates. Further, about one third of galaxies are removed due to contamination of their spectra by other sources in the field. Of the galaxies above the flux and extraction limits, the fraction remaining as part of the final selection are listed in black. Our sample contains 2676 galaxies from 0.7<z<1.5 spanning two decades in M$_*$ and SFR.

2. DATA

2.1. *The 3D-HST Survey*

We investigate the spatial distribution of star formation in galaxies during the epoch spanning $0.7 < z < 1.5$ across the $SFR - M_*$ plane using data from the 3D-HST survey. 3D-HST is a 248 orbit extragalactic treasury program with HST furnishing NIR imaging and grism spectroscopy across a wide field (van Dokkum et al. 2011; Brammer et al. 2012a, Momcheva et al. in prep). HST's G141 grism on Wide Field Camera 3 (WFC3) provides spatially resolved spectra of all objects in the field of view. The G141 grism has a wavelength range of $1.15\mu m < \lambda < 1.65\mu m$, covering the Hα emission line for $0.7 < z < 1.5$. Combined with the accompanying H_{F140W} imaging, 3D-HST enables us to derive the spatial distribution of Hα and rest-frame R-band emission with matching 1 kpc resolution for an objectively selected sample of galaxies.

The program covers the well-studied CANDELS fields (Grogin et al. 2011; Koekemoer et al. 2011) AEGIS, COSMOS, GOODS-S, UDS, and also includes GOODS-N (GO-11600, PI: B. Weiner.) The optical and NIR imaging from CANDELS in conjunction with the bountiful public photometric data from $0.3 - 24\mu m$ provide stringent constraints on the spectral energy distributions (SEDs) of galaxies in these fields (Skelton et al. 2014).

2.2. *Determining z, M$_*$, SFR*

This study depends on robustly determining galaxy integrated properties, specifically M$_*$ and SFR. Both of these quantities in turn depend on a robust determination of redshift and constraints on the spectral energy distributions of galaxies across the electro-magnetic spectrum. To do this, the photometric data was shepherded and aperture photometry was performed to construct psf-matched, deblended,

$J_{F125W}/H_{F140W}/H_{F160W}$ selected photometric catalogs (see Skelton et al. 2014). These photometric catalogs form the scaffolding of this project upon which all the remaining data products rest. For this study, we rely on the rest-frame colors, stellar masses, and star formation rates. All of these quantities were derived based on constraints from across the electromagnetic spectrum.

Our redshift fitting method also utilizes the photometry. This is probably not strictly necessary for the sample of Hα line emitting galaxies used for this study, although it helps to confirm the redshift of galaxies with only one emission line detected. It is crucial, however, for galaxies without significant emission or absorption features falling in the grism spectrum. To measure redshifts, the photometry and the two-dimensional G141 spectrum were fit simultaneously with a modified version of the EAzY code (Brammer, van Dokkum, & Coppi 2008). After finding the best redshift, emission line strengths were measured for all lines that fall in the grism wavelength range (see Momcheva et al. in prep).

Galaxy stellar masses were derived using stellar population synthesis modeling of the photometry with the FAST code (Kriek et al. 2009). We used the Bruzual & Charlot (2003) templates with solar metallicity and a Chabrier (2003) initial mass function. We assumed exponentially declining star formation histories and the Calzetti et al. (2000) dust attenuation law (see Skelton et al. 2014). Errors in the stellar mass due to contamination of the broadband flux by emission lines are not expected to be significant for this study (see appendix in Whitaker et al. 2014).

Galaxy star formation rates in this work were computed by summing unobscured (UV) plus dust absorbed and re-emitted

emission (IR) from young stars:

$$\mathrm{SFR} = \mathrm{SFR}_{UV+IR}(M_\odot yr^{-1}) = 1.09 \times 10^{-10}(L_{IR}+2.2L_{UV})/L_\odot \tag{1}$$

(Bell et al. 2005). L_{UV} is the total UV luminosity from 1216 – 3000 Å. It is derived by scaling the rest-frame 2800 Å luminosity determined from the best-fit SED with EAzY (Brammer et al. 2008). L_{IR} is the total IR luminosity from $8 - 1000\mu$m. It is derived by scaling the MIPS 24μm flux density using a luminosity-independent template that is the log average of the Dale & Helou (2002) templates with $1 < \alpha < 2.5$ (Wuyts et al. 2008; Franx et al. 2008; Muzzin et al. 2010). See Whitaker et al. (2014) for more details.

2.3. *Sample Selection*

We consider all galaxies 1) in the redshift range $0.7 < z < 1.5$ for which the Hα emission line falls in the G141 grism wavelength coverage; 2) that have stellar masses $9.0 < \log(M_*) < 11.0$, a mass range over which our H–band selected catalogs are complete; and 3) that are characterized as star-forming according to the UVJ-color criterion based on SED shape (Labbe et al. 2005; Wuyts et al. 2007; Whitaker et al. 2011). The UVJ selection separates quiescent galaxies from star forming galaxies using the strength of the Balmer/4000Å break which is sampled by the rest-frame $U-V$ and $V-J$ colors. These three criteria result in a parent sample of 8068 star-forming galaxies. The grism spectra are fit down to $H_{F140W} = 24$, trimming the sample to 6612.

We select galaxies based on a quite generous cut in Hα Flux: $F(\mathrm{H}\alpha) > 3 \times 10^{-17}$erg/s/cm^2, This limit corresponds to a median signal to noise $S/N(\mathrm{H}\alpha) = 2$ and sample of 4314 galaxies. Galaxies with lower Hα fluxes were removed as they may have larger redshift errors. We note here that this sample is Hα-limited, not Hα-selected. That is, it is a mass-selected sample of star-forming galaxies where we require an Hα flux to ensure only galaxies with correct redshifts are included. As a result of the flux and grism extraction limits, we are less complete at low masses and star formation rates. We exclude 178 galaxies which were flagged as having bad GALFIT (Peng et al. 2002) fits in the van der Wel et al. (2014a) catalogs, often indicative of oddities in the photometry. We identify galaxies that are likely to host active galactic nuclei (AGN) as sources with X-ray luminosity $L_x > 10^{42.5}$erg s^{-1} or Hα emission line widths of $\sigma > 1000$ km/s (see next section). We remove these 57 galaxies from the sample as emission from AGN would complicate the interpretation of the measured Hα distributions.

Finally, of this sample, we discard 34% of galaxies due to contamination of their spectra by the spectra of other nearby objects (see next section for more detail). The contaminating spectra are primarily bright stars and galaxies unrelated to the object, but it is possible that this criterion might lead to a slight bias against denser environments. The fraction of galaxies removed from the sample due to contamination does not vary with stellar mass or star formation rate. The final sample contains 2676 galaxies and is shown in Fig. 1.

3. ANALYSIS

3.1. *Morphological Information in the Spectrum*
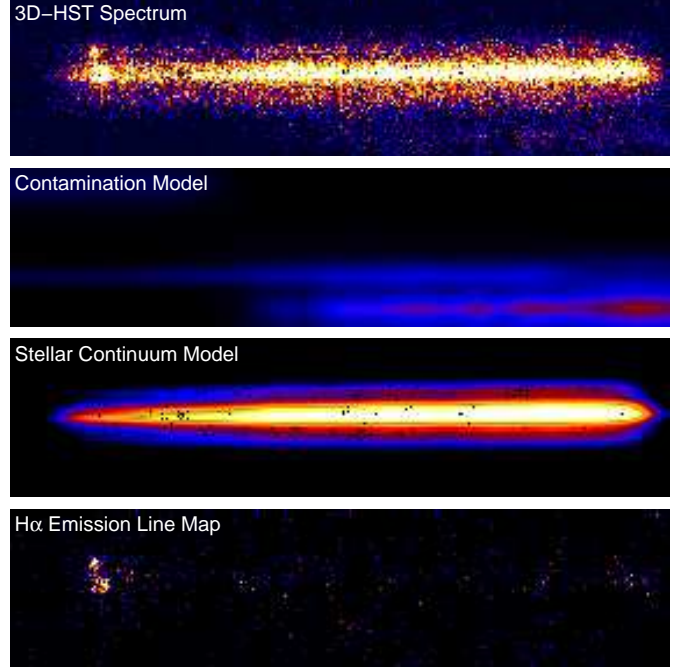

FIG. 2.— Illustration of the creation of Hα emission line maps from HST WFC3 grism data. The top panel shows the 2D, interlaced grism spectrum. The second panel shows a model for the "contamination": the spectra of all objects in the field except the object of interest. The third panel is a 2D model for the continuum emission of the galaxy. The bottom panel is the original spectrum with the contaminating emission from other obejcts, and the stellar continuum, subtracted. The result is a 2D map of the line emission at the spatial resolution of HST (see Sect. 3.2 for details).

The Hα maps at the heart of this analysis are created from the two-dimensional 3D-HST grism spectra. The creation of Hα emission line maps is possible as a consequence of a unique interaction of features: WFC3 has high spatial resolution ($0.''14$) and the G141 grism has low ($R\sim130$) point source spectral resolution. A G141 grism spectrum is a series of high resolution images of a galaxy taken at 46Å increments and placed next to each other on the WFC3 detector. An emission line in such a set up effectively emerges as an image of the galaxy in that line superimposed on the continuum. A resolution element for a galaxy at $z \sim 1$ corresponds to a velocity dispersion of $\sigma \sim 1000$ km/s, so a spectrum will only yield velocity information about a galaxy if the velocity difference across that galaxy is more than 1000 km/s . Few galaxies have such large line widths. Thus in general, structure in an emission line is due to *morphology*, not kinematics. While in a typical ground based spectroscopy, the shape of the emission line yields spectral information, in our spectra it yields spatial information. The upshot of this property is that by subtracting the continuum from a spectrum, we obtain an emission line map of that galaxy. A sample G141 spectrum is shown in Fig. 2 and sample Hα maps are shown in Fig. 3.

We note that although it is generally true that the spectral axes of these Hα maps do not contain kinematic information, there is one interesting exception: broad line AGN. With line widths of > 1000km/s, the spectra of these objects do contain kinematic information. These sources are very easy to pick
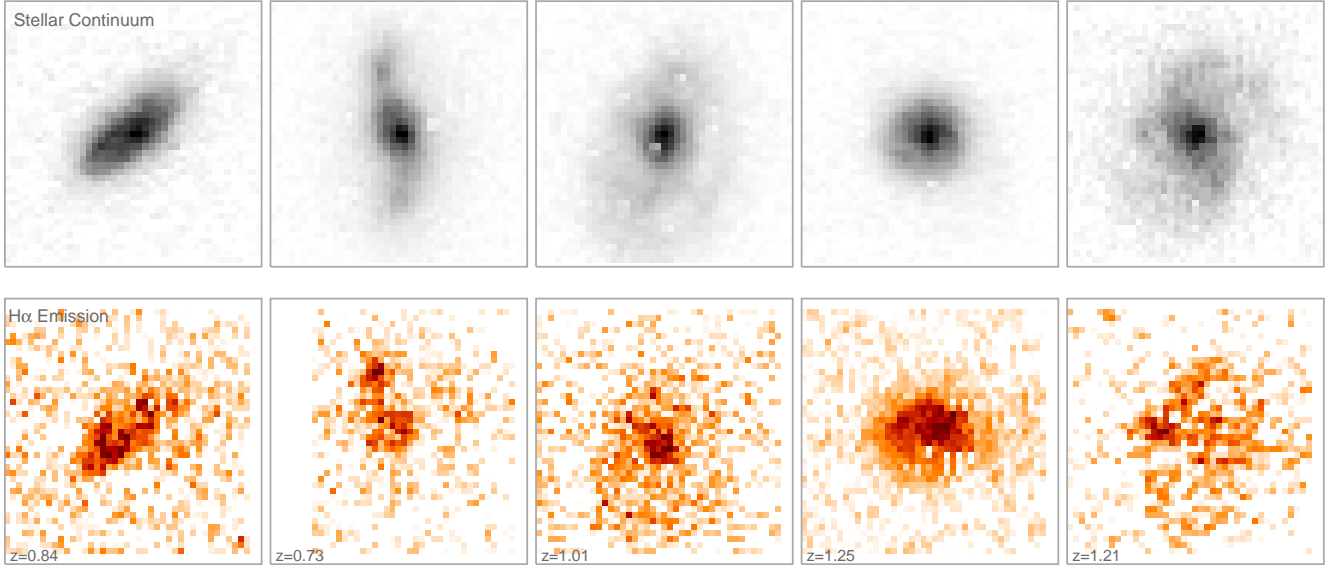
Fig. 3.— High resolution Hα maps for $z \sim 1$ galaxies from HST and their corresponding rest-frame optical images. The Hα generally follows the optical light but not always (see also Wuyts et al. 2013).

out: they appear as point sources in the spatial direction and extended in the spectral direction.

Furthermore, because the WFC3 camera has no slits, we get a 2D spectrum of every object in the camera's field of view. For all galaxies with $0.7<z<1.5$, that have an Hα emission line in G141's wavelength coverage, we obtain an Hα map to the surface brightness limits. Based on our selection criteria, using this methodology, we have a sample of 2676 galaxies at $0.7<z<1.5$ with spatially resolved Hα information.

3.2. *Making Hα maps*

The reduction of the 3D-HST spectroscopy with the G141 grism and imaging with the H_{F140W} filter was done using a custom pipeline. HST data is typically reduced by drizzling, but the observing strategy of 3D-HST allows images to be interlaced instead. With this dither pattern, four images are taken with pointing offsets that are multiples of half pixels. The pixels from these four uncorrected frames are then placed on an output grid with 0.06" pixels (van Dokkum et al. 2000). Interlacing improves the preservation of spatial information, effectively improving the spatial resolution of the images. Crucially, interlacing also eliminates the correlated noise caused by drizzling. This correlated noise is problematic for analysis of spectroscopic data because it can masquerade as spectral features.

Although the background levels in NIR images taken from space are lower than in those taken from earth, they are still significant. The modeling of the background in the grism data is complicated because it is composed of many faint higher order spectra. It is done using a linear combination of three physical eigen-backgrounds: zodiacal light, metastable He emission (Brammer et al. 2014), and scattered light from the Earth limb (Brammer et al. in prep). Residual background structure in the wavelength direction of the frames is fit and subtracted along the image columns. (For more information see Brammer et al. 2012a, 2014, Momcheva et al. in prep) The 2D spectra are extracted from the interlaced G141 frames around a spectral trace based on a geometrical mapping from

the location of their F140W direct image positions. A sample 2D spectrum and a pictorial depiction of the remainder of this subsection is shown in Fig. 2.

The advantage of slitless spectroscopy is also its greatest challenge: flux from neighboring objects with overlapping traces can contaminate the spectrum of an object with flux that does not belong to it. We forward-model contamination with a flat spectrum based on the direct image positions and morphologies of contaminating objects. A second iteration is done to improve the models of bright ($H < 22$) sources using their extracted spectra. An example of this contamination model is shown in the second panel of Fig. 2 (See Brammer et al. 2012a, 2012b, 2013, Momcheva et al. in prep). To remove contamination from the spectra, we subtract these models for all galaxies in the vicinity of the object of interest. Furthermore, for the present analysis, all regions predicted to have contamination which is greater than a third of the average G141 background value were masked. This aggressive masking strategy was used to reduce the uncertainty in the interpretation of the Hα maps at large radii where uncertainties in the contamination model could introduce systematics.

The continuum of a galaxy is modeled by convolving the best fit SED without emission lines with its combined $J_{F125W}/H_{F140W}/H_{F160W}$ image. The continuum model for our example galaxy is shown in the third panel of Fig. 2. This continuum model is subtracted from the 2D grism spectrum, removing the continuum emission and simultaneously correcting the emission line maps for stellar absorption. What remains for galaxies with $0.7 < z < 1.5$ is a map of their Hα emission. Five sample Hα maps and their corresponding H_{F140W} images are shown in Fig. 3. Crucially, the Hα and stellar continuum images were taken with the same camera under the same conditions. This means that differences in their spatial distributions are intrinsic, not due to differences in the PSF. The spatial resolution is ~ 1 kpc for both the H_{F140W} stellar continuum and Hα emission line maps.

The final postage stamps we use in this analysis are 80×80 pixels. An HST pixel is 0.06", so this corresponds to $4.8 \times$

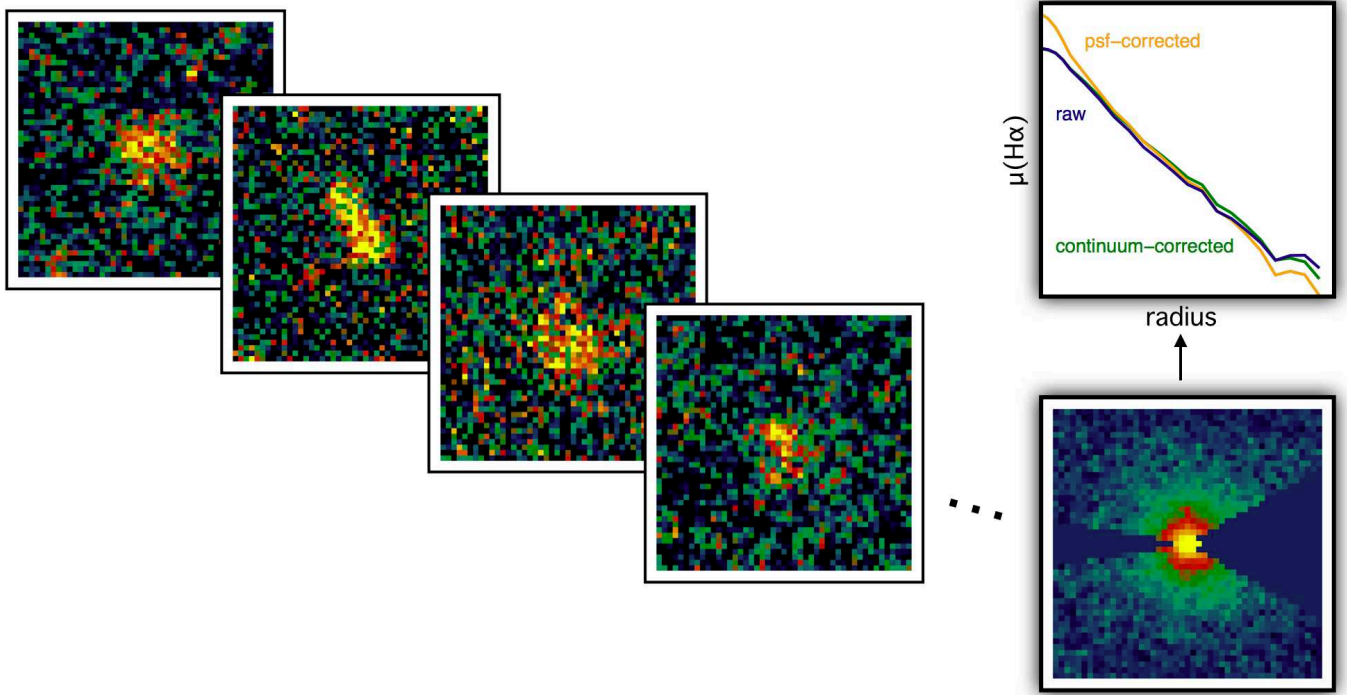FIG. 4.— Illustration of the creation of Hα image stack and the derivation of radial profiles. The panels on the left show four of the 377 Hα maps that are summed to create the stack on the right. The stack is masked with the "double pacman" mask shown, in order to mitigate the effects of redshift uncertainties and [S II] $\lambda\lambda 6716, 6731$Å (see § 3.3). The surface brightness profiles derived from this stack are shown above it. The raw profile is shown in black. The profile corrected for residual continuum is shown in green and the profile corrected for the effects of the psf is shown in orange.

4.8" or 38×38 kpc at $z \sim 1$. Many of these postage stamps have a small residual positive background (smaller than the noise). To correct for this background, we compute the median of all unmasked pixels in the 2 kpc edges of each stamp and subtract it. This means that we can reliably trace the surface brightness out to 17 kpc. Beyond this point, the surface brightness is definitionally zero.

3.3. *Stacking*

To measure the average spatial distribution of Hα during this epoch from $z = 1.5 - 0.7$, we create mean Hα images by stacking the Hα maps of individual galaxies with similar M_* and/or SFR (See § 4 & 5). Many studies first use Hα images of individual galaxies to measure the spatial distribution of star formation then describe average trends in this distribution as a function of M_* or SFR (e.g., Förster Schreiber et al. 2006; Epinat et al. 2009; Förster Schreiber et al. 2009; Genzel et al. 2011; Nelson et al. 2012; Epinat et al. 2012; Contini et al. 2012; Wuyts et al. 2013; Genzel et al. 2014a). Instead, we first create average Hα images by stacking galaxies as a function M_* and SFR then measure the spatial distribution of star formation to describe trends. This stacking strategy leverages the strengths of our data: Hα maps taken under uniform observing conditions for a large and objectively defined sample of galaxies. From a practical standpoint, the methodology has the advantage that we do not need data with very high signal-to-noise. As a consequence, we can explore relatively uncharted regions of parameter space. In particular, we can measure the radial distribution of star formation in galaxies across a vast expanse of the SFR-M_* plane down to low masses and star formation rates. Additionally, we can probe the distribution of ionized gas in the outer regions of galaxies where star formation surface densities are thought to be very low.

We created the stacked images by summing normalized, masked images of galaxies in H_{F140W} and Hα. To best control for the various systematics described in the remainder of this section, for our primary analysis, we do not distort the galaxy images by de-projecting, rotating, or scaling them. We show major-axis aligned stacks in § 6 and de-projected, radially-normalized profiles in an appendix. Our results remain qualitatively consistent regardless of this methodological decision. For all analyses, the images were weighted by their H_{F140W} flux so the stack is not dominated by a single bright object. The H_{F140W} filter covers the full wavelength range of the G141 grism encompassing the Hα emission line. Normalizing by the H_{F140W} emission hence accounts for very bright Hα line emission without inverse signal-to-noise weighting as normalizing by the Hα emission would.

As a consequence of the grism's low spectral resolution, we have to account for the blending of emission lines. With a FWHM spectral resolution of ~ 100 Å, Hα $\lambda 6563$Å and [N II] $\lambda 6548 + 6583$Å are blended. To account for the contamination of Hα by [N II], we scale the measured flux down by a factor of 1.15 (Sanders et al. 2015) and adopt this quantity as the Hα flux. This is a simplistic correction as [N II]/Hα varies between galaxies (e.g. Savaglio et al. 2005; Erb et al. 2006b; Maiolino et al. 2008; Zahid et al. 2013; Leja et al. 2013; Wuyts et al. 2014; Sanders et al. 2015; Shapley et al. 2015) as well as radially within galaxies (e.g. Yuan et al. 2011; Queyrel et al. 2012; Swinbank et al. 2012; Jones et al. 2013, 2015; Förster Schreiber et al. 2014; Genzel et al. 2014b; Stott et al. 2014). Stott et al. (2014) find a range of metallicity gradients $-0.063 < \Delta Z / \Delta r < 0.073$ dex kpc^{-1}, with the median of ~ 0 (no gradient) for 20 typical star-

forming galaxies at $z \sim 1$. Hence, we choose to adopt a single correction factor so as not to introduce systematic uncertainties into the data.

Additionally, Hα $\lambda6563$Å and [S II] $\lambda\lambda6716,6731$Å are resolved but are separated by only ~ 3 resolution elements. In this study, we are concerned primarily with the radial distribution of Hα emission. In order to prevent [S II] from adding flux at large radii, we mask the region of the 2D spectrum redward of Hα where [S II] emission could contaminate the Hα maps.

Galaxies are centered according to the light-weighted center of their H_{F140W} flux distribution. Given that the H_{F140W} can be used as a proxy for stellar mass, we chose to center the galaxies according to their H_{F140W} center as our best approximation of centering them according to stellar mass. While the H_{F140W} centroid will not always be the exact center of mass, it is a better estimate than our other option, the Hα centroid. We measure the centroid of the H_{F140W} images as the flux-weighted mean pixel in the x- and y- directions independently with an algorithm similar to the iraf task imcntr. We shift the H_{F140W} image with sub-pixel shifts using damped sinc interpolation. The G141 image is shifted with the same shifts. To center the Hα map requires only a geometric mapping in the spatial direction of 2D grism spectrum. In the spectral direction, however, the redshift of a galaxy and the spatial distribution of its Hα are degenerate. As a result, the uncertainty in the spectral direction of the Hα maps is ~ 0.5 pixels (see Brammer et al. 2012a).

To simultaneously address these problems, we apply an asymmetric double pacman mask to the Hα maps. This mask is shown applied to the stack in Fig. 4. The mask serves three purposes. First, it masks the [S II] emission which otherwise could masquerade as Hα flux at large radii. Second, it mitigates the effect of the redshift-morphology degeneracy by removing the parts of the Hα distribution that would be most affected. Third, it reduces the impact of imperfect stellar continuum subtraction by masking the portion of the spectrum that would be most afflicted.

A mask was also created for each galaxy's H_{F140W} image to cover pixels that are potentially affected by neighboring objects. This mask was constructed from the 3D-HST photometric data products. SExtractor was run on the combined $J_{F125W}/H_{F140W}/H_{F160W}$ detection image (see Skelton et al. 2014). Using the SExtractor segmentation map, we flagged all pixels in a postage stamp belonging to other objects and masked them. For both Hα and H_{F140W} a bad pixel mask is created for known bad or missing pixels as determined from the data quality extensions of the fits files.

The final mask for each Hα image is comprised of the union of three separate masks: 1) the bad pixel mask, 2) the asymmetric double pacman mask, and 3) the contamination mask (see previous section). A final H_{F140W} mask is made from the combination of two separate masks 1) the bad pixel mask and 2) the neighbor mask. The Hα and H_{F140W} images are multiplied by these masks before they are summed. Summing the masks creates what is effectively a weight map for the stacks. The raw stacks are divided by this weight map to create the final exposure-corrected stacked images.

3.4. *Surface brightness profiles*

The stacked Hα image for galaxies with $10^{10} < M_* < 10^{10.5}$ is shown in Fig. 4. With hundreds of galaxies, this image is very deep and we can trace the distribution of Hα out to large radii ($\sim 10\,$kpc). To measure the average radial profiles of the

Hα and H_{F140W} emission, we compute the surface brightness as a function of radius by measuring the mean flux in circular apertures. We checked that the total flux in the stacks matched the Hα and H_{F140W} fluxes in our catalogs. We compute error bars on the radial profiles by bootstrap resampling the stacks and in general, we cut off the profiles when $S/N < 2.5$. The Hα profile for the example stack is shown in Fig. 4. Before moving on to discussing the trends in the observed radial profiles, we note two additional corrections made to them.

First, we correct the continuum model used to create the Hα maps. This continuum model goes out to the edge of the segmentation map of each galaxy, which typically encompasses $\gtrsim 95\%$ of the light. We subtract the remaining continuum flux by correcting the continuum model to have the same spatial distribution as the broad band light. The H_{F140W} filter covers the same wavelength range as the G141 grism. Therefore, the radial distribution of H_{F140W} emission reflects the true radial distribution of continuum emission. We derive a correction factor to the continuum model of each stack by fitting a second degree polynomial to the radial ratio of the H_{F140W} stack to the stacked continuum model. This continuum correction is $< 20\%$ at all radii in the profiles shown here.

Second, we correct the radial profiles for the effect of the PSF. Compared to typical ground-based observations, our space-based PSF is narrow and relatively stable. We model the PSF using Tiny Tim (Krist 1995) and interlacing the model PSFs in the same way as the data. The FWHM is 0.14", which corresponds to $\sim 1\,$kpc at $z \sim 1$. Although this is small, it has an effect, particularly by blurring the centers of the radial profiles. Images can be corrected using a deconvolution algorithm. However, there are complications with added noise in low S/N regions and no algorithm perfectly reconstructs the intrinsic light distribution (see e.g. van Dokkum et al. 2010). We instead employ the algorithmically more straight-forward method of Szomoru et al. (2010). This method takes advantage of the GALFIT code which convolves models with the PSF to fit galaxy light distributions (Peng et al. 2002). We begin by fitting the stacks with Sérsic (1968) models using GALFIT (Peng et al. 2002). These Sérsic fits are quite good and the images show small residuals. We use these fit parameters to create an unconvolved model. To account for deviations from a perfect Sérsic fit, we add the residuals to this unconvolved image. Although the residuals are still convolved with the PSF, this method has been shown to reconstruct the true flux distribution even when the galaxies are poorly fit by a Sérsic profile (Szomoru et al. 2010). It is worth noting again that the residuals in these fits are small so the residual-correction step in this procedure is not critical to the conclusions of this paper.

4. THE DISTRIBUTION OF Hα AS A FUNCTION OF STELLAR MASS AND RADIUS

The structure of galaxies (e.g. Wuyts et al. 2011a; van der Wel et al. 2014a) and their sSFRs (e.g. Whitaker et al. 2014) change as a function of stellar mass. This means that both where a galaxy is growing and how rapidly it is growing depend on how much stellar mass it has already assembled. In this section, we investigate where galaxies are building stellar mass by considering the average radial distribution of Hα emission in different mass ranges.

To measure the average spatial distribution of Hα during this epoch from $z = 1.5 - 0.7$, we create mean Hα images by stacking the Hα maps of individual galaxies as described in § 3.3. The stacking technique employed in this paper serves

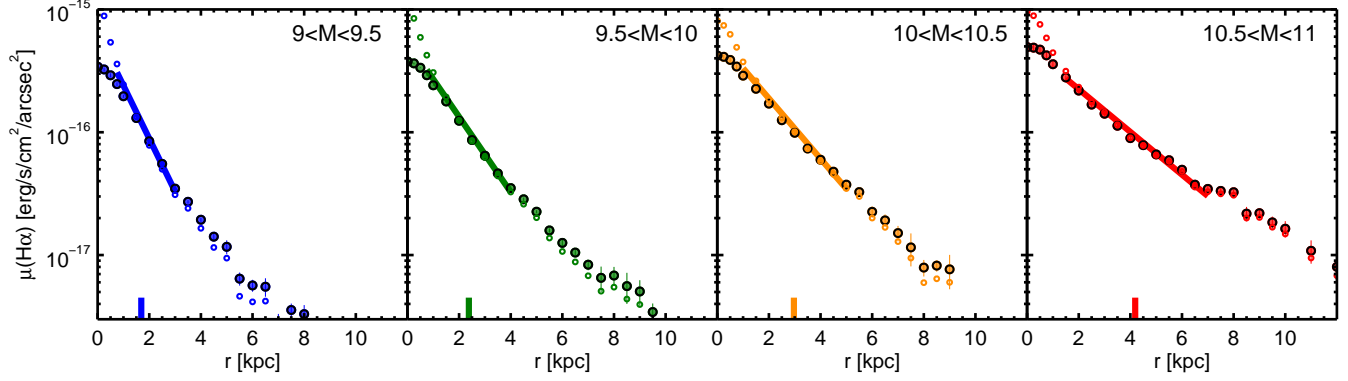FIG. 5.— The average radial distribution of Hα emission in galaxies in bins of stellar mass indicated at the top of each panel. The filled circles show the radial profiles measured directly from the stacked Hα images. The open circles show the profiles corrected for the effect of the PSF. The lines show the best fit exponentials for $0.5r_s < r < 3r_s$ to the PSF-corrected profiles. There appears to be some excess flux over a pure exponential at small and large radii. The short vertical lines show the corresponding Hα effective radii.
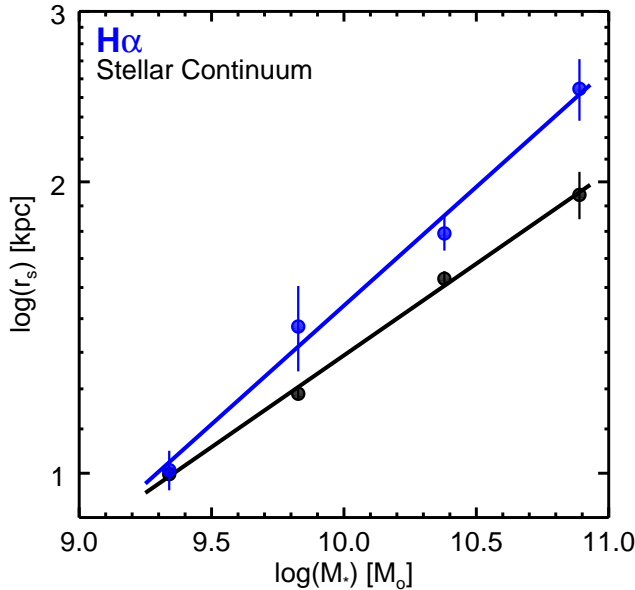

FIG. 6.— Size-mass relations for Hα $(r_{H\alpha} - M_*)$ stellar continuum $(r_* - M_*)$. The size of star forming disks traced by Hα increases with stellar mass as $r_{H\alpha} \propto M^{0.23}$. At low masses, $r_{H\alpha} \sim r_*$, as mass increases the disk scale length of Hα becomes larger than the stellar continuum emission as $r_{H\alpha} \propto r_* M_*^{0.054}$. Interpreting Hα as star formation and stellar continuum as stellar mass, this serves as evidence that on average, galaxies are growing larger in size due to star formation.

to increase the S/N ratio, enabling us to trace the profile of Hα to large radii. An obvious disadvantage is that the Hα distribution is known to be different for different galaxies. As an example, the Hα maps of the galaxies shown in Fig. 3 are quite diverse, displaying a range of sizes, surface densities, and morphologies. Additionally, star formation in the early universe often appears to be clumpy and stochastic. Different regions of galaxies light up with new stars for short periods of time. These clumps, while visually striking, make up a small fraction of the total star formation at any given time. Only 10−15% of star formation occurs in clumps while the remaining 85−90% of star formation occurs in a smooth disk or bulge component (Förster Schreiber et al. 2011b; Wuyts et al.

2012, 2013). Stacking Hα smoothes over the short-timescale stochasticity to reveal the time-averaged spatial distribution of star formation.

Fig. 5 shows the radial surface brightness profiles of Hα as a function of stellar mass. The first and most obvious feature of these profiles is that the Hα is brightest in the center of these galaxies: the radial surface brightness of Hα rises monotonically toward small radii. The average distribution of ionized gas is not centrally depressed or even flat, it is centrally peaked. This shows that there is substantial on-going star formation in the centers of galaxies at all masses at $z \sim 1$.

With regard to profile shape, in log(flux)-linear(radius) space, these profiles appear to be nearly linear indicating they are mostly exponential. There is a slight excess at small and large radii compared to an exponential profile. However, the profile shape is dependent on the stacking methodology: if the profiles are deprojected and normalized by their effective radius (as derived from the H_{F140W} data) they are closer to exponential (see appendix). We do not use these normalized profiles as the default in the analysis, as it is difficult to account for the effects of the PSF.

We quantify the size of the ionized gas distribution in two ways: fitting exponential profiles and Sérsic models. For simplicity, we measure the disk scale lengths ($\equiv r_s$) of the ionized gas by fitting the profiles with an exponential between $0.5r_s < r < 3r_s$. These fits are shown in Fig. 5. It is clear that over the region $0.5r_s < r < 3r_s$ the Hα distribution is reasonably well-approximated by an exponential. Out to $5r_s$, $\sim 90\%$ of the Hα can be accounted for by this single exponential disk fit. This implies that most of the Hα lies in a disk.

The scale length of the exponential disk fits increases with mass from 1.3 kpc for $9.0 < M_* < 9.5$ to 2.6 kpc for $10.5 < M_* < 11.0$. With $r_e = 1.678r_s$, this corresponds to effective (half-light) radii of 2.2 kpc and 4.4 kpc respectively. We fit the size-mass relation of the ionized gas disks $(r_{H\alpha} - M_*)$ with:

$$r_{H\alpha}(m_*) = 1.5m_*^{0.23} \qquad (2)$$

where $m_* = M_*/10^{10}M_\odot$. Fitting the H_{F140W} surface brightness profiles in the same way shows the exponential disk scale lengths of the stellar continuum emission vs. the ionized gas. We parameterize this comparison in terms of the stellar continuum size:
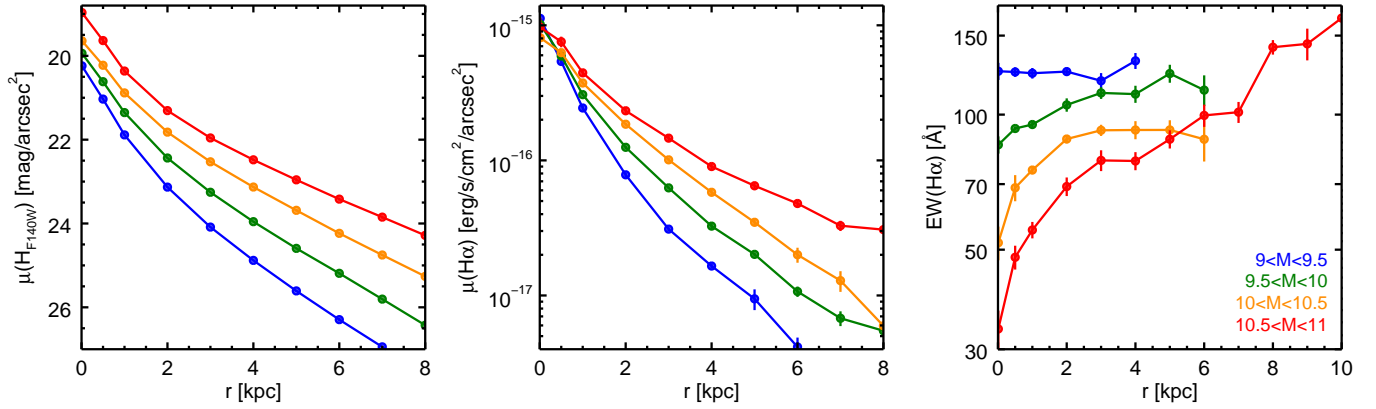
$$r_*(m_*) = 1.4m_*^{0.18} \qquad (3)$$

FIG. 7.— Average radial surface brightness profiles of H_{F140W} (left), Hα (center), and average radial Hα equivalent width profile (EW(Hα)) (right) in galaxies as a function of stellar mass. The radial EW(Hα) profile is the quotient of the Hα and stellar continuum profiles, providing a comparison between the spatial distribution of Hα and stellar continuum emission. At low masses the EW(Hα) profile is flat. As mass increases EW(Hα) rises increasingly steeply from the center, showing, in agreement with the larger disk scale lengths of Fig. 6, that the Hα has a more extended distribution than the existing stellar continuum emission.

$$r_{H\alpha}(m_*, r_*) = 1.1 \, r_* \, (m_*^{0.054}) \qquad (4)$$

For $10^9 M_\odot < M_* < 10^{9.5} M_\odot$, the H$\alpha$ emission has the same disk scale length as the H_{F140W} emission. This suggests that the Hα emission closely follows the H_{F140W} emission (or possibly the other way around). At stellar masses $M_* > 10^{9.5}$ the scale length of the Hα emission is larger than the H_{F140W}. As mass increases, the Hα grows increasingly more extended and does not follow the H_{F140W} emission as closely. The size-mass relations for Hα and H_{F140W} are shown in Fig. 6.

The ionized gas distributions can also be parameterized with Sérsic profiles. We fit the observed, PSF-convolved stacks with Sérsic models using GALFIT as described in the previous section. The Sérsic index of each, which reflects the degree of curvature of the profile, is $1 < n < 2$ for all mass bins, demonstrating that they are always disk-dominated. The Sérsic indices and sizes measured with GALFIT are listed in Table 1. The sizes measured with GALFIT are similar to those measured using exponential disk fits and exhibit the same qualitative trends.

While the bootstrap error bars for each individual method are very small, $2-4\%$, different methodologies result in systematically different size measurements. We derive our default sizes by fitting exponentials to the $0.5r_s < r < 3r_s$ region of PSF-corrected profiles. Fit the same way, sizes are $10-20\%$ larger when profiles are not corrected for the PSF. Adopting slightly different fitting regions can also change the sizes by $10-20\%$. The GALFIT sizes are $3-15\%$ larger. With all methods the trends described remain qualitatively the same. That is, the effective radius of the Hα emission is always greater or equal to the effective radius of the H_{F140W} and both increase with stellar mass.

The comparison between the radial distribution of Hα and H_{F140W} can be seen explicitly in their quotient, the radial Hα equivalent width (EW(Hα)) profile (Fig. 7), indicating where the Hα emission is elevated and depressed relative to the H_{F140W} emission. The first and most obvious feature is that the normalization of equivalent width profiles decreases with increasing stellar mass, consistent with spatially-integrated results (Fumagalli et al. 2012) and the fact that sSFR declines with stellar mass (e.g. Whitaker et al. 2014). Additionally, below a stellar mass of $\log(M)_* < 9.5$, the equivalent width profile is flat, at least on the scales of ~ 1kpc

TABLE 1
STRUCTURAL PARAMETERS

$\log(M_*)$	Hα			H_{F140W}		
	r_s	r_e	n	r_s	r_e	n
$9.0 < \log(M_*) < 9.5$	1.0	1.8	1.9	1.0	1.8	1.9
$9.5 < \log(M_*) < 10.0$	1.5	2.7	1.8	1.3	2.4	1.9
$10.0 < \log(M_*) < 10.5$	1.8	3.2	1.5	1.6	3.1	1.7
$10.5 < \log(M_*) < 11.0$	2.6	5.1	1.7	2.0	3.9	2.1

Note. Disk scale length and effective radius in kpc and Sérsic index for Hα and H_{F140W} as a function of stellar mass. For an exponential disk (n=1), $r_e = 1.678 r_s$.

resolved by our data. These galaxies are growing rapidly across their disks. In addition to the overall normalization of the EW decreasing, as stellar mass increases the shape of the EW profile changes, its slope growing steeper. For $9.5 < \log(M_*) < 10.0$, EW(Hα) rises by a factor of ~ 1.3 from the center to $2r_e$, for $10.5 < \log(M_*) < 11.0$, it rises by $\gtrsim 3$. At low masses, the entire disk is illuminated with new stars; at higher masses, the Hα is somewhat centrally depressed relative to the stellar continuum emission. Consistent with the measured size trends, the radial EW(Hα) profiles show that Hα has a similar distribution as the stellar continuum emission for $9.0 < \log(M_*) < 9.5$; as mass increases Hα becomes more extended and less centrally concentrated than the stellar continuum emission.

Interpreting Hα as star formation and H_{F140W} as stellar mass implies that star formation during the epoch $0.7 < z < 1.5$ is building galaxies from the inside-out as discussed in § 7.3.

5. THE RADIAL DISTRIBUTION OF Hα ACROSS THE STAR FORMING SEQUENCE

In the previous section, we showed how the radial distribution of star formation depends on the stellar mass of a galaxy. Here we show how it depends on the total star formation rate at fixed mass. In other words, we show how it depends on a galaxy's position in the SFR-M_* plane with respect to the star forming main sequence. (The star forming 'main sequence' is an observed locus of points in the SFR-M_* plane Brinchmann et al. 2004; Zheng et al. 2007; Noeske et al. 2007; Elbaz
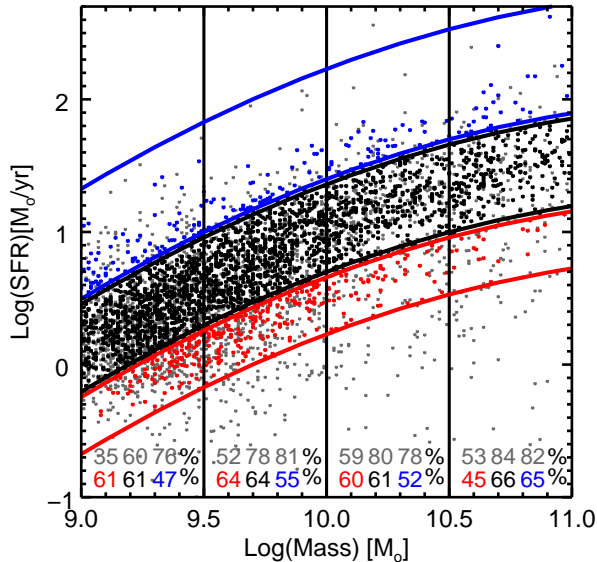
FIG. 8.— We investigate the spatial distribution of star formation in galaxies across the SFR(UV+IR)-M$_*$ plane. To do this, we stack the Hα maps of galaxies on the star forming sequence main sequence (black) and compare to the spatial distribution of Hα in galaxies above (blue) and below (red) the main sequence. The parent sample is shown in gray. The fractions of the total parent sample above the Hα flux and extraction magnitude limit are listed at the bottom in gray. As expected, we are significantly less complete at low masses, below the main sequence. About one third of selected galaxies are thrown out of the stacks due to contamination of their spectra by other sources in the field. Of the galaxies above the flux and extraction limits, the fractions remaining as part of the the final selection are listed and shown in blue/black/red and respectively.

et al. 2007; Daddi et al. 2007; Salim et al. 2007; Damen et al. 2009; Magdis et al. 2010; González et al. 2010; Karim et al. 2011; Huang et al. 2012; Whitaker et al. 2012, 2014)

5.1. *Definition of the Star Forming Main Sequence*

We define the star forming sequence according to the results of Whitaker et al. (2014), interpolated to $z = 1$. The slope of the relation between SFR and M$_*$ decreases with M$_*$, as predicted from galaxy growth rates derived from the evolution of the stellar mass function (Leja et al. 2015), reflecting the decreased efficiency of stellar mass growth at low and high masses. Whitaker et al. (2014) find that the observed scatter is a constant $\sigma = 0.34$ dex with both redshift and M$_*$.

We investigate where 'normal' star-forming galaxies were forming their stars at this epoch by determining the radial distribution of Hα in galaxies on the main sequence. We elucidate how star formation is enhanced and suppressed in galaxies by determining where star formation is "added" in galaxies above the main sequence and "subtracted" in galaxies below the main sequence. To determine where star formation is occurring in galaxies in these different regions of the SFR-M$_*$ plane, we stack Hα maps as a function of mass and SFR. We define the main sequence as galaxies with SFRs $\pm 1.2\sigma = \pm 0.4$ dex from the Whitaker et al. (2014) main sequence line at $z \sim 1$. Specifically, we consider galaxies 'below', 'on', or 'above' the star forming main sequence to be the regions [-0.8,-0.4] dex, [-0.4,+0.4] dex, or [+0.4,+1.2] dex with respect to the main sequence line in the SFR-M$_*$ plane. To define these regions consistently we normalize the SFRs of all galaxies to $z \sim 1$ using the redshift evolution of the normalization of the star forming sequence from Whitaker et al.

(2012). These definitions are shown pictorially by Fig. 8 in red, black, and blue respectively. We imposed the +1.2 dex upper limit above the main sequence so the stacks wouldn't be dominated by a single, very bright galaxy. We impose the -0.8 dex due to the Hα flux-driven completeness limit. Fig. 8 also shows which galaxies were actually used in the stacks. Our broad band magnitude extraction limit and Hα flux limit manifest themselves as incompleteness primarily at low masses and SFRs as reflected in the gray numbers and filled symbols.

We adopted this $\pm 1.2\sigma$ definition of the main sequence to enable us to probe the top and bottom 10% of star formers and ferret out differences between galaxies growing very rapidly, very slowly, and those growing relatively normally. According to our definition ($\pm 1.2\sigma$), the 'Main Sequence' accounts for the vast majority of galaxy growth. It encompasses 80% of UVJ star-forming galaxies and 76% of star formation. The star forming main sequence is defined by the running median star formation rate of galaxies as a function of mass. The definition is nearly identical when the mode is used instead, indicating that it defines the most common rate of growth. While we left 20% of star-forming galaxies to probe the extremes of rapid and slow growth, only 7% of these galaxies live above the main sequence and nearly double that, 13%, live below it. This is a manifestation of the fact that the distribution of star formation rates at a given mass is skewed toward low star formation rates. Counting galaxies, however, understates the importance of galaxies above the main sequence to galaxy evolution because they are building stellar mass so rapidly. Considering instead the contribution to the total star formation budget at this epoch, galaxies above the main sequence account for $> 20\%$ of star formation while galaxies below the main sequenceonly account for $< 3\%$.

5.2. *Results*

One of the primary results of this paper is shown in Fig. 9: the radial distribution of Hα on, above and below the star forming main sequence. Above the main sequence, Hα is elevated at all radii. Below the main sequence, Hα is depressed at all radii. The profiles are remarkably similar above, on, and below the main sequence – a phenomenon that can be referred to as 'coherent star formation', in the sense that the offsets in the star formation rate are spatially-coherent. As shown in and Fig. 10, the offset is roughly a factor of 2 and nearly independent of radius: at $r < 2$ kpc the mean offset is a factor of 2.2, at $3 < r < 5$ kpc it is a factor of 2.1. Above the main sequence at the highest masses where we have the signal-to-noise to trace the Hα to large radii, we can see that the Hα remains enhanced by a factor of $\gtrsim 2$ even beyond 10 kpc. The most robust conclusion we can draw from the radial profiles of Hα is that star formation from $\sim 2-6$ kpc is enhanced in galaxies above the main sequence and suppressed in galaxies below the main sequence (but see § 7.4 for further discussion).

We emphasize that the SFRs used in this paper were derived from UV+IR emission, These star formation rate indicators are measured independently from the Hα flux. Thus, it is not a priori clear that the Hα emission is enhanced or depressed for galaxies above or below the star forming main sequence as derived from the UV+IR emission. The fact that it is implies that the scatter in the star forming sequence is real and caused by variations in the star formation rate (see § 7.4).

In the middle panels of Fig. 9 we show the radial profiles of H_{F140W} emission as a function of M$_*$ above, on, and below the star forming main sequence. As expected, we find that
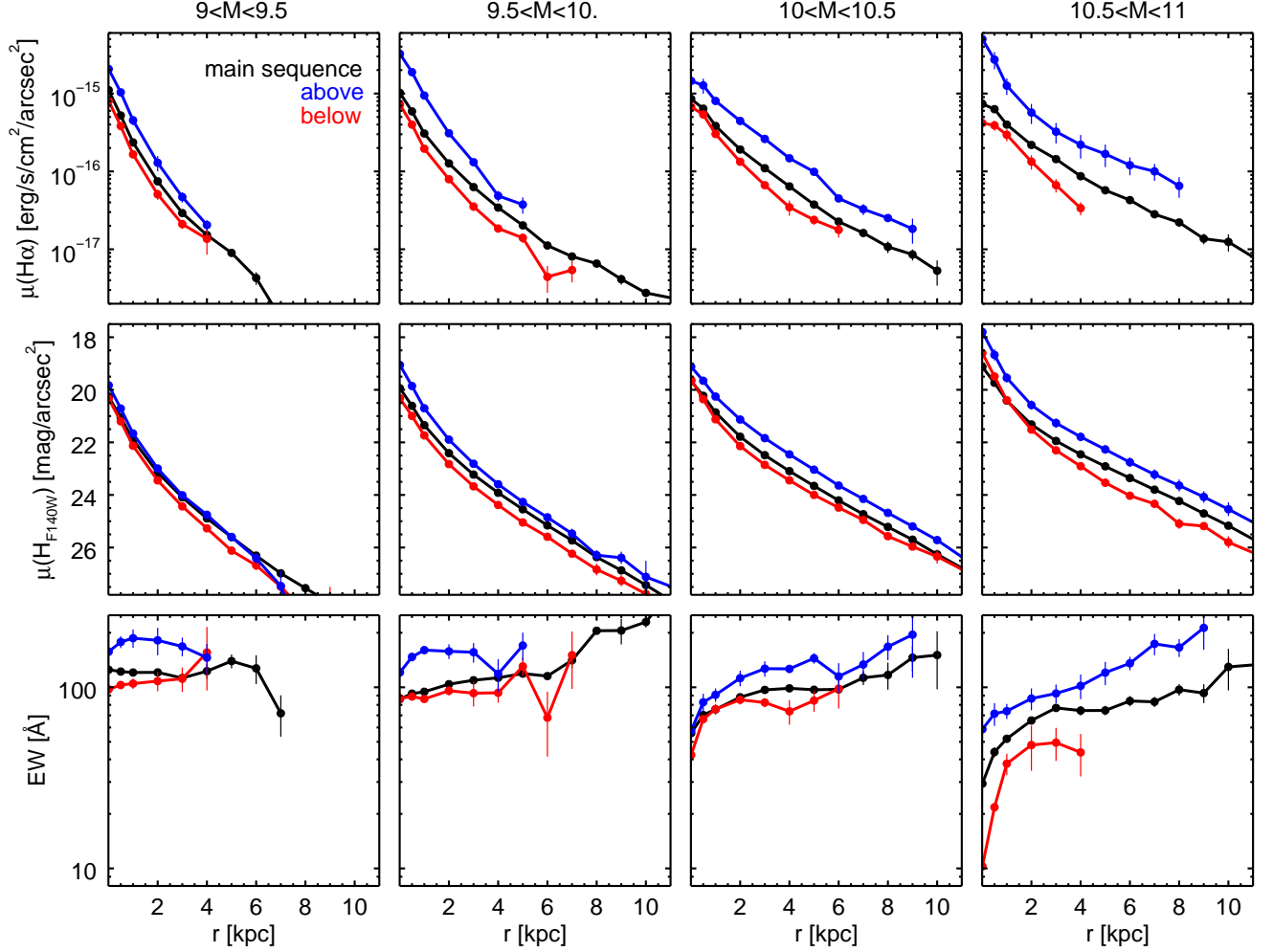
Fig. 9.— Radial surface brightness profiles of Hα, H_{F140W}, and their ratio EW(Hα) as a function of M_* and SFR. The colors delineate position with respect to the star forming 'main sequence': above (blue), on (black), and below (red). Above the star forming main sequence, the Hα (as well as the H_{F140W} and EW(Hα) is elevated at all radii. Below the star forming main sequence, the Hα is depressed at all radii. The average radial profiles are always centrally peaked in Hα and never centrally peaked in EW(Hα).

the average sizes and Sérsic indices of galaxies increase with increasing stellar mass. Disk scale lengths of Hα and H_{F140W} are listed in Table 2. At high masses, we find that above and below the main sequence, the H_{F140W} is somewhat more centrally concentrated than on the main sequence (consistent with Wuyts et al. 2011a; Lang et al. 2014, Whitaker et al. in prep), possibly indicating more dominant bulges below and above the main sequence. We note that these trends are less obvious at lower masses. Furthermore, as one would expect, the mass to light ratio decreases with sSFR because young stars are brighter than old stars. Therefore, at fixed mass, galaxies above the main sequence have brighter H_{F140W} stellar continuum emission and galaxies below the main sequence have fainter H_{F140W} emission.

In the bottom panels of Fig. 9 we show the radial EW(Hα) profiles. The most obvious feature of these profiles is that EW(Hα) is *never* centrally peaked. EW(Hα) is always flat or centrally depressed, indicating the Hα is always equally or less centrally concentrated than the the H_{F140W} emission. Above the main sequence, the EW(Hα) is elevated at all radii. Below the main sequence, the EW(Hα) is depressed at most radii. These trends are discussed more extensively in § 7.4-5,

where we convert the EW(Hα) profiles to sSFR profiles.

6. EFFECTS OF ORIENTATION

In the previous sections we analyzed average images and radial profiles of Hα emission with galaxies stacked as they were oriented on the detector. This methodology has the advantage that it allows for better control of systematics. In particular, we can effectively subtract the continuum out to large radii as we can use the radial distribution of the H_{F140W} flux to correct for the ≤ 5% of flux missing from the continuum models. A galaxy's position angle on the detector, however, is arbitrary and has no physical meaning.

Here we present stacks of galaxies rotated to be aligned along the major axis, as measured from the continuum emission. This is an important test of the idea that the Hα emission originates in disks that are aligned with the stellar distribution: in that case these rotated Hα stacks should have similar axis ratios as the rotated H_{F140W} stacks. We divide the galaxies into the same mass bins as in the previous sections, and compare the most face-on vs. the most edge-on galaxies. The position angle and projected axis ratio ($q = B/A$) of each galaxy is measured from its H_{F140W} image using GAL-

TABLE 2
DISK SCALE LENGTHS OF Hα AND STELLAR CONTINUUM EMISSION BELOW, ON, AND ABOVE THE STAR FORMING MAIN SEQUENCE

	$r_s(H\alpha)$ [kpc]			$r_s(H_{F140W})$ [kpc]		
$\log(M_*)$	below	MS	above	below	MS	above
$9.0 < \log(M_*) < 9.5$	1.43 ± 0.28	1.24 ± 0.06	1.12 ± 0.06	1.17 ± 0.03	1.24 ± 0.01	1.17 ± 0.03
$9.5 < \log(M_*) < 10.0$	1.44 ± 0.07	1.68 ± 0.02	1.20 ± 0.15	1.46 ± 0.03	1.51 ± 0.01	1.27 ± 0.09
$10.0 < \log(M_*) < 10.5$	1.90 ± 0.14	1.99 ± 0.05	1.95 ± 0.08	1.78 ± 0.08	1.83 ± 0.02	1.82 ± 0.09
$10.5 < \log(M_*) < 11.0$	1.68 ± 0.11	2.60 ± 0.08	3.14 ± 0.49	1.57 ± 0.02	2.22 ± 0.05	1.86 ± 0.13

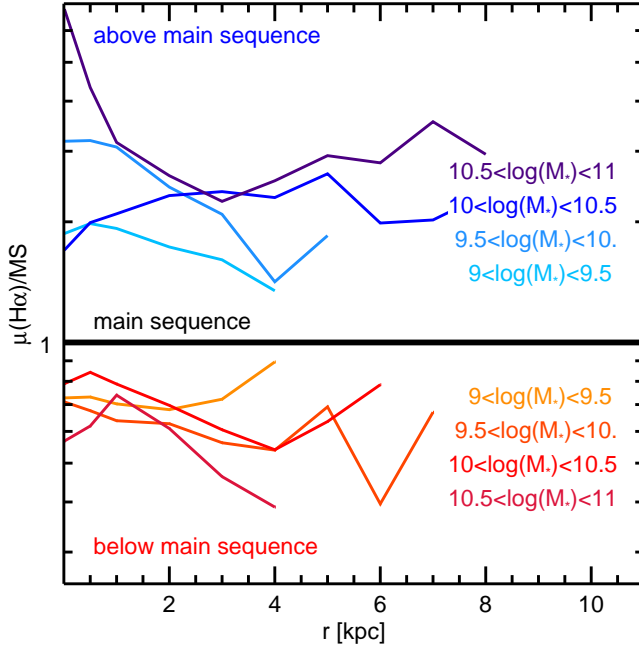* For an exponential disk (n=1), the half-light radius is $r_e = 1.678 r_s$.

FIG. 10.— Radial profiles of Hα as a function of mass normalized by the main sequence radial profile (MS). Above the star forming main sequence, the Hα is elevated at all radii (blue hues). Below the star forming main sequence, the Hα is depressed at all radii (red hues).

FIT (Peng et al. 2002). We rotate the H_{F140W} and Hα images according to their H_{F140W} position angle to align them along the major axis. In each mass bin, we then create face- and edge-on stacks from the galaxies with the highest and lowest 20% in projected axis ratio, respectively.

The distribution of projected axis ratios is expected to be broad if most galaxies are disk-dominated (see, e.g., van der Wel et al. 2014b). If we interpret the galaxy images as disks under different orientations, we would expect the stacks of galaxies with the highest 20% of projected axis ratios to have an average axis ratio of ~ 0.9 and the stacks of galaxies with the lowest 20% of projected axis ratios to be flattened with average axis ratios of ~ 0.3 (see van der Wel et al. 2014b). As shown in Fig. 11 the rotated H_{F140W} stacks are consistent with this expectation. Furthermore, the rotated Hα stacks are qualitatively very similar to the rotated H_{F140W} stacks, which means that the Hα emission is aligned with that of the stars.

For the edge-on stacks, we measure the flattening of the Hα emission and compare it to that of the H_{F140W} emission. In the four mass bins, from low mass to high mass, we find $q(H\alpha) = [0.29 \pm 0.02, 0.32 \pm 0.03, 0.31 \pm 0.02, 0.37 \pm 0.02]$ and $q(H_{F140W}) = [0.28 \pm 0.01, 0.27 \pm 0.01, 0.29 \pm 0.01, 0.34 \pm$

0.01] respectively, where the errors are determined from bootstrap resampling. We find that the average axis ratio of H_{F140W} emission is $q(H_{F140W}) = 0.295 \pm 0.005$ and $q(H\alpha) = 0.323 \pm 0.011$. We conclude that the Hα is slightly less flattened than the H_{F140W} emission, but the difference is only marginally significant.

There are physical reasons why Hα can have an intrinsically larger scale height than the H_{F140W} emission. Given that outflows are ubiquitous in the $z \sim 2$ universe (e.g. Shapley et al. 2003; Shapiro et al. 2009; Genzel et al. 2011; Newman et al. 2012; Kornei et al. 2012; Förster Schreiber et al. 2014; Genzel et al. 2014a), it is possible that the Hα would have a larger scale height due winds driving ionized gas out of the plane of the stellar disk. Furthermore, attenuation towards HII regions could be more severe in the midplane of the disk than outside of it. This would result in Hα emission being less concentrated around the plane of the disk, giving a larger scale height. Finally, the gas disks and the stellar disks can be misaligned. The fact that the edge-on Hα and H_{F140W} stacks are so similar shows that all these effects are small.

At a more basic level, an important implication of the similarity of the Hα stacks and the H_{F140W} stacks is that it directly shows that we are not stacking noise peaks. If we were just stacking noise, a stack of galaxies flattened in H_{F140W} would not be flattened in Hα because the noise would not know about the shape of the H_{F140W} emission. It is remarkable that this holds even for the lowest mass stack, which contains the galaxies with the lowest Hα S/N ratio as well as the smallest disk scale lengths.

7. DISCUSSION

Thus far, we have only discussed direct observables: H_{F140W} and Hα. In this Section we explicitly interpret the radial profiles of Hα as radial profiles of star formation and the radial profiles of H_{F140W} as radial profiles of stellar surface density.

7.1. Interpreting Hα and H_{F140W} as SFR and Mass

In §4 and §5, we showed the radial distribution of Hα, H_{F140W}, and EW(Hα). Hα emission is typically used as a tracer of star formation, H_{F140W} (rest-frame optical) emission as a proxy for stellar mass, and EW(Hα) for the specific star formation rate (sSFR) (e.g. Förster Schreiber et al. 2011a; Wuyts et al. 2013; Genzel et al. 2014b; Tacchella et al. 2015b, 2015a). We do the same here to gain more physical insight into the observed profiles. If we assume that Hα traces star formation and H_{F140W} traces stellar mass, the profiles can be scaled to these physical quantities using the integrated values. To derive mass surface density profiles, we ignore M/L gradients and apply the integrated M_*/L_{F140W} as a constant scale factor at all radii. Similarly, to derive star formation sur-
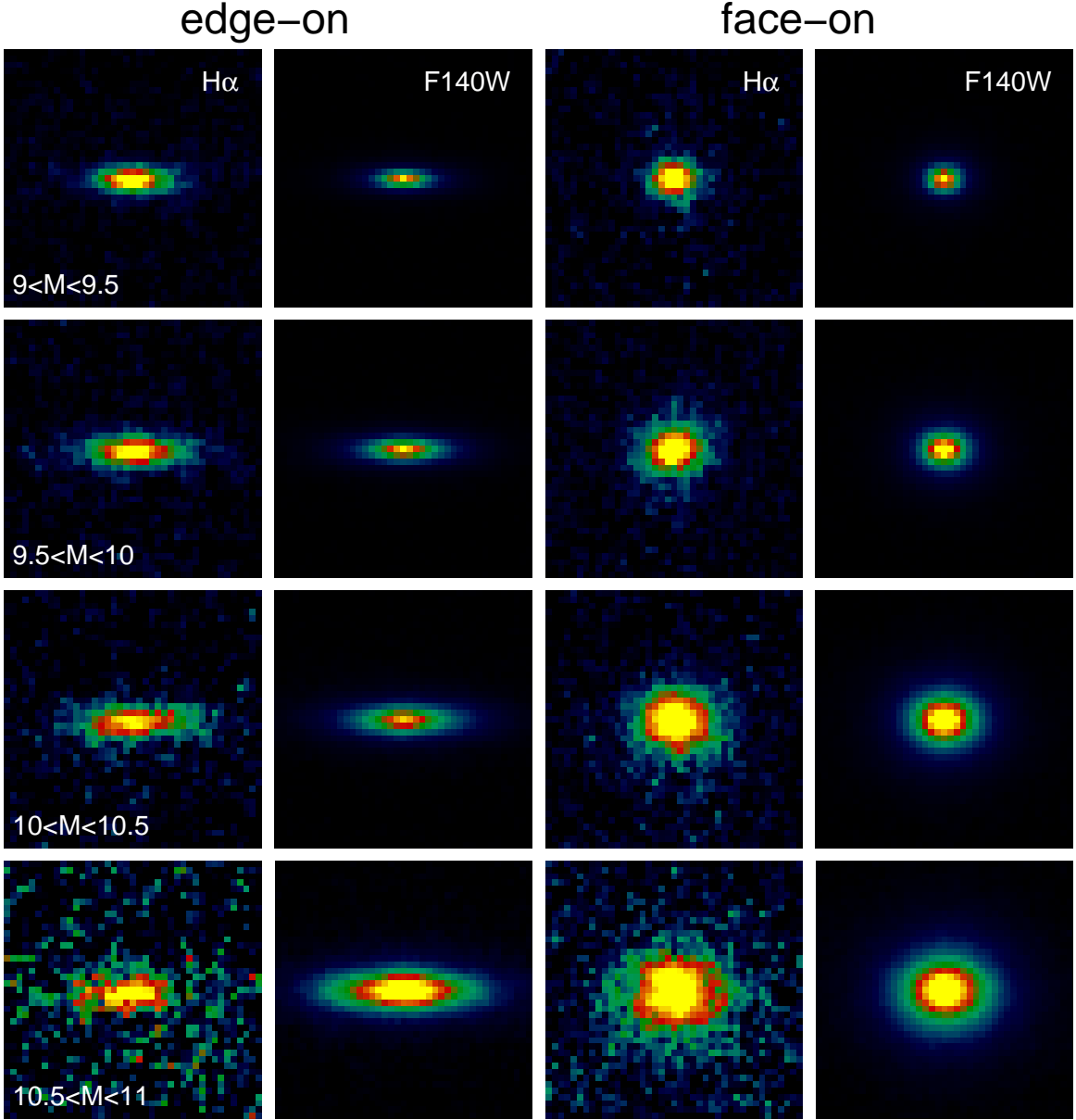
FIG. 11.— Stacks of galaxies after rotating them so their major axes are aligned, for the 20 % of galaxies with the lowest ellipticities ("face-on") and the 20 % of galaxies with the highest ellipticiticies ("edge-on"). The lowest ellipticity stacks are nearly round and the highest ellipticity stacks are highly flattened with $a/b \approx 0.3$, consistent with viewing disks under different projections. The Hα stacks are remarkably similar to the H_{F140W} stacks, demonstrating that the Hα emission is aligned with the H_{F140W} emission at all masses.

face density profile, we ignore radial dust gradients and scale the Hα profiles based on the integrated $SFR(UV+IR)/L_{H\alpha}$ ratio. The sSFR profile is then the quotient of the SFR and M_* profiles. However, there are a number of caveats associated with interpreting the H_{F140W}, Hα, and EW(Hα) profiles in this manner.

We first assess the assumption that there are no radial gradients in the SFR/Hα ratio. This assumption can be undermined in four ways: dust, AGN, winds, and metallicity, which have opposing effects. Dust will increase the SFR/Hα ratio by obscuring the ionizing photons from star forming regions. AGN, winds, and higher metallicity will reduce the SFR/Hα ratio, as they add ionizing photons that do not trace star formation.

These aspects, and hence the extent to which a scaling from Hα to SFR is a good assumption, themselves depend on stellar mass and star formation rate. Dust attenuation is correlated with stellar mass (e.g. Reddy et al. 2006, 2010; Pannella et al. 2009; Wuyts et al. 2011b; Whitaker et al. 2012; Momcheva et al. 2013). At fixed mass, dust attenuation is also correlated with star formation rate (Wang & Heckman 1996; Adelberger & Steidel 2000; Hopkins et al. 2001; Reddy et al. 2006, 2010; Wuyts et al. 2011b; Sobral et al. 2012; Domínguez et al. 2013; Reddy et al. 2015). Within galaxies, dust attenuation is anti-correlated with radius (e.g., Wuyts et al. 2012), as it depends on the column density. This means that SFR and Hα should trace each other reasonably well for low mass

galaxies with low star formation rates, and particularly poorly in the the centers of massive, rapidly star-forming galaxies (Nelson et al. 2014; van Dokkum et al. 2015). The same qualitative scalings with mass and star formation likely apply to the likelihood of an AGN being present, outflows, and the contamination of Hα by [N II]. That is, AGN are most likely to haunt the centers of massive, rapidly star-forming galaxies (e.g., Rosario et al. 2013; Förster Schreiber et al. 2014; Genzel et al. 2014a). [N II]/Hα is most likely to be enhanced above the assumed value in the centers of massive galaxies (as described in §3.3). Shocks from winds may contribute to the Hα emission in the central regions, particularly at high masses (Newman et al. 2012; Förster Schreiber et al. 2014; Genzel et al. 2014a). The takeaway here is that we are relatively confident interpreting Hα as star formation at low masses, low SFRs, and all profiles outside of the center. We are less confident for the centers of the radial profiles of massive or highly star-forming galaxies.

Next, we assess the assumption that there is no radial gradient in the M/L ratio. Dust and AGN affect the M/L in the same way as SFR/Hα although less strongly (e.g. Calzetti et al. 2000; Wuyts et al. 2013; Marsan et al. 2015; Reddy et al. 2015). Galaxies growing inside-out will also have gradients in their stellar population ages. Since older stellar populations have higher M/L ratios, these age gradients translate into M/L gradients. Age and dust increase M_*/H_{F140W} and AGN decrease it. Hence using H_{F140W} as a proxy for M_* is a fairly safe assumption at lower masses where age and dust gradients are small and AGN are rare. It is somewhat less certain at high masses. We also note that the contribution of the Hα emission to the total H_{F140W} flux is small, $\sim 5\%$.

As the EW(Hα) profile is the quotient of the Hα and H_{F140W} interpreting it as a profile of sSFR is accompanied by the amalgam of all of the above uncertainties: dust, age, AGN, and metallicity. This does not necessarily mean that the sSFR profile is more uncertain than the profiles of star formation and mass, as some effects cancel. In a two component dust model (e.g. Calzetti, Kinney, & Storchi-Bergmann 1994; Charlot & Fall 2000), the light from both stars and HII regions is attenuated by diffuse dust in the ISM. The light from the HII regions is attenuated additionally by dust in the undissipated birth clouds. Because the continuum and line emission will be affected equally by the diffuse dust, the EW(Hα) profile will only be affected by the extra attenuation toward the stellar birth clouds, not the totality of the dust column. As a consequence, the effect of dust on the EW(Hα) profiles is mitigated relative to the Hα profiles. The quantity of extra attenuation towards HII regions remains a matter of debate with estimates ranging from none (Erb et al. 2006a; Reddy et al. 2010) to a factor of 2.3 (Calzetti et al. 2000; Yoshikawa et al. 2010; Wuyts et al. 2013) and many in between (e.g., Förster Schreiber et al. 2009; Wuyts et al. 2011b; Mancini et al. 2011; Kashino et al. 2013). As with the total attenuation, the quantity of extra attenuation toward HII regions appears to increase with M_* and SFR (Price et al. 2014; Reddy et al. 2015). Reddy et al. (2015) find that extra attenuation becomes significant at SFR$\sim 20 M_\odot$/yr. If true, extra extinction should be taken into account for galaxies on the main sequence at the highest masses, and above the main sequence at $\log(M_*) > 9.5$. The issue should be less acute for galaxies with low masses and SFRs. The only way to definitively resolve this question is to obtain spatially-resolved dust maps in the future.

7.2. Star formation in disks

The center panel of Fig. 12 shows the radial distribution of SFR as a function of stellar mass derived by scaling the Hα profiles to the total SFR(UV+IR). The radial distribution of SFR is consistent with being disk-dominated: as discussed in § 4, an exponential provides a reasonably good fit to the profiles and the Sérsic indices are $1 < n < 2$. Out to $7r_s$, $\sim 85\%$ of the Hα can be accounted for by a single exponential disk fit. Approximately 15% of the Hα emission is in excess above an exponential: 5% from the center ($< 0.5r_s$) and 10% from large radii ($> 3r_s$).

Taken at face value the shape of the stacked Hα profiles suggests that the star formation during the epoch $0.7 < z < 1.5$ mostly happens in disks with the remainder building central bulges and stellar halos. In reality, of course, the universe is likely much more complicated. Radial dust gradients will make the star formation appear less centrally concentrated. Stacking galaxies of different sizes will make the star formation appear more centrally concentrated, as shown in the appendix. Additionally, the gas that Hα traces can be ionized by physical processes other than star formation such as AGN, winds, or shock heating from the halo. So with the Hα we observe we may also be witnessing the growth of black holes, excited gas being driven out of galaxies, or the shock heating of the inflowing gas that fuels star formation.

Interestingly, a common feature of the Hα profiles is that they all peak at the center. If we interpret the Hα as star formation, this means that at all masses, galaxies are building their centers. Although we caution that shocks from winds and AGN could add Hα (Förster Schreiber et al. 2014; Genzel et al. 2014a) and dust attenuation could subtract Hα from the centers of the profiles. That we observe Hα to be centrally peaked was not necessarily expected: recently it was found that some massive galaxies at $z \sim 2$ have Hα rings (see e.g. Genzel et al. 2014b; Tacchella et al. 2015a), which have been interpreted as evidence for inside-out quenching. We note that our averaged profiles do not exclude the possibility that some individual galaxies have rings at $z \sim 1$, which are offset by galaxies with excess emission in the center.

7.3. Inside-out Growth

The star formation surface density (as traced by Hα) is always centrally peaked but the sSFR (as traced by EW(Hα)) is never centrally peaked. Confirming Nelson et al. (2013) we find that, in general, EW(Hα) is lower in the center than at larger radii. Confirming Nelson et al. (2012), we find that the effective radius of the Hα emission is generally larger than the effective radius of the H_{F140W} emission. This means that the Hα emission is more extended and/or less centrally concentrated than the H_{F140W} emission. If Hα traces star formation and H_{F140W} traces stellar mass, these results indicate that galaxies have radial gradients in their specific star formation rates: the sSFR increases with radius. If the centers are growing more slowly than the outskirts, galaxies will build outward, adding proportionally more stars at larger radii. This suggests that star formation is increasing the size of galaxies. However, galaxies are still building significantly at their centers (probably even more than we see due to the effects of dust) consistent with the fact that size growth due to star formation appears to be fairly weak (van Dokkum et al. 2013; van der Wel et al. 2014a; van Dokkum et al. 2015).

Additionally, there appears to be a trend in $r_s(H\alpha)/r_s(H_{F140W})$ with mass. Below $3 \times 10^9 M_\odot$, the
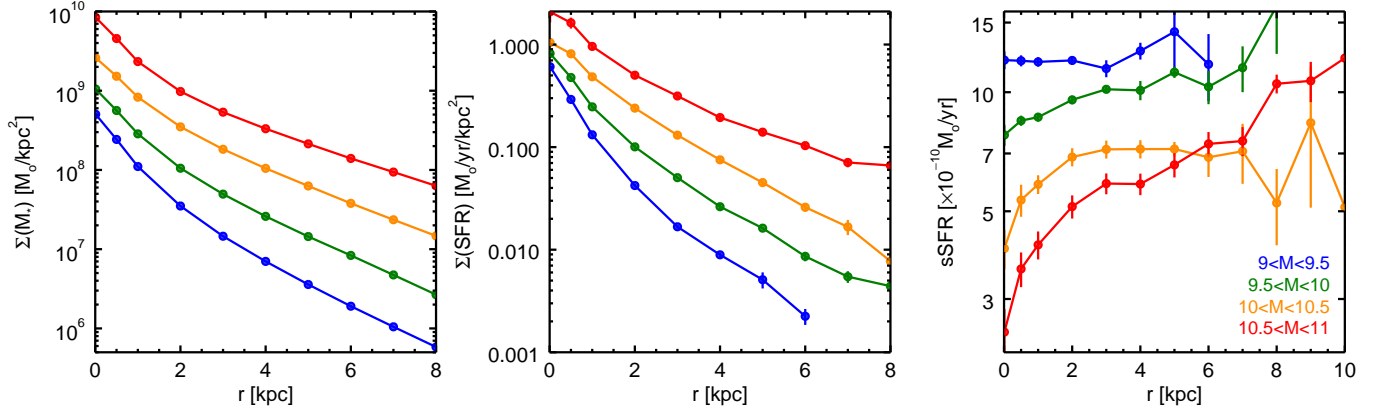
FIG. 12.— Stellar mass surface density(left), star formation surface density(center), and specific star formation rate (right) as a function of radius and stellar mass. These profiles were made by scaling the profiles of Hα, H_{F140W}, and EW(Hα) in Fig. 7 to SFR, M$_*$, and sSFR. Within galaxies, the specific star formation rate rises radially; the star formation is more extended than the existing stellar mass. This is a direct demonstration that galaxies at this epoch grow inside-out.

Hα and the H_{F140W} roughly trace each other: the radial EW profile is flat and $r_s(H\alpha) \sim r_s(H_{F140W})$. As mass increases, H$\alpha$ becomes more extended than the H_{F140W} emission: the EW(Hα) profile is increasingly centrally depressed and $r_s(H\alpha) > r_s(H_{F140W})$. This reflects the natural expectations of inside out growth and the shape of the sSFR-M$_*$ relation from both a physical and an observational standpoint.

Observationally, our tracers Hα and H_{F140W} may trace somewhat different things as a function of increasing stellar mass. At the low mass end, because low mass galaxies have such high sSFRs, it's possible that the H_{F140W} emission is dominated by light from young stars and is not actually a good tracer of stellar mass. This means that there may in fact be a difference in the disk scale lengths of the stellar mass and star formation but it is hard to detect because our proxy for M$_*$ is dominated by the youngest stars. At the high mass end, galaxies have more dust so star formation could be preferentially obscured at small radii. Consequently, the Hα could appear to be less centrally concentrated than the star formation is in reality, making the inferred size larger (see e.g. Simpson et al. 2015). Taken together, these effects could contribute to the trend of increasing $r_s(H\alpha)/r_s(H_{F140W})$ with stellar mass. However, as described in § 7.1, there are a number of other observational effects that work in the opposite direction, decreasing the $r_s(H\alpha)/r_s(H_{F140W})$ at high masses. Dust will also obscure the stellar continuum emission, meaning that the stellar mass could also be more concentrated than observed. Age gradients will also change the M/L ratio, again adding more stellar mass at the center. Szomoru et al. (2013) estimate that galaxies are $\sim$ 25% more compact in mass than in light. AGN contributing line emission to the Hα profiles will also work to decrease this ratio by adding extra flux and decreasing the size of the star formation. In sum, it seems more likely that observational effects will increase the $r_s(H\alpha)/r_s(H_{F140W})$ with mass (and generally) than decrease it but as the effects act in both directions we cannot say with certainty which are more important.

While many observational effects could contribute to the mass dependence of the size ratio, this effect may also have a physical explanation. More massive galaxies have older mean ages. This means that a larger fraction of their star formation took place at earlier cosmic times. Hence, it is perhaps then reasonable that their stellar mass – the integral of their past star formation history – would be more

compact than the gas disks with ongoing star formation. On the other hand, low mass galaxies have younger mean ages, which means their mass-weighted sizes are closer to the sizes of their star forming disks.

7.4. *Above and Below the Main Sequence*

Here we return to the profiles above and below the star-forming main sequence, that is, for galaxies with relatively high and relatively low star formation rates for their stellar mass. Whitaker et al. (2012) showed that the SEDs of galaxies above and below the main sequence are different from those on it. Above the main sequence, the SEDs are dusty but blue which they interpreted as indicative of AGN or merger-induced starbursts. Below the main sequences, the SEDs are not dusty but red, which they interpreted as indicative of star formation being shut down. Additionally, Wuyts et al. (2011a) showed that galaxies above and below the main sequence were structurally more compact and centrally concentrated than galaxies on the star forming main sequence.

Hints as to what physical processes are driving a galaxy above or below the main sequence are given by these trends in stellar structure and SED shape. The next key piece of information is *where* the star formation is enhanced above and suppressed below the star forming sequence, which we show here. For instance, if the primary physical processes driving galaxies above the main sequence are AGN or central starbursts, we would expect Hα to be enhanced in the center but not at larger radii. If quenching is driven by processes acting from the center and progressing from the inside outward, we would galaxies below the main sequence to have a decrease in Hα primarily in the center.

We characterize galaxies with respect to the star formation main sequence using their total SFR(IR+UV)s which reflect the total obscured+unobscured ionizing flux from young stars. As described in §5.2, we find that above the main sequence, the Hα is enhanced at all radii; below the above the main sequence the Hα is depressed at all radii. In Fig. 13 we show SFR, M$_*$, and sSFR profiles made by scaling our Hα profiles using the integrated SFR(IR+UV)/SFR(Hα) and H_{F140W} profiles using the integrated M$_*/L_{F140W}$ with all the associated caveats described in §7.1. Because the integrated M$_*/L_{F140W}$ decreases with increasing SFR at fixed mass, the offset in the H_{F140W} light profiles shown in middle panels of Fig. 9 disappears in the M$_*$ profiles shown middle panels of Fig. 13. At fixed mass, galaxies are brighter above the main sequence and
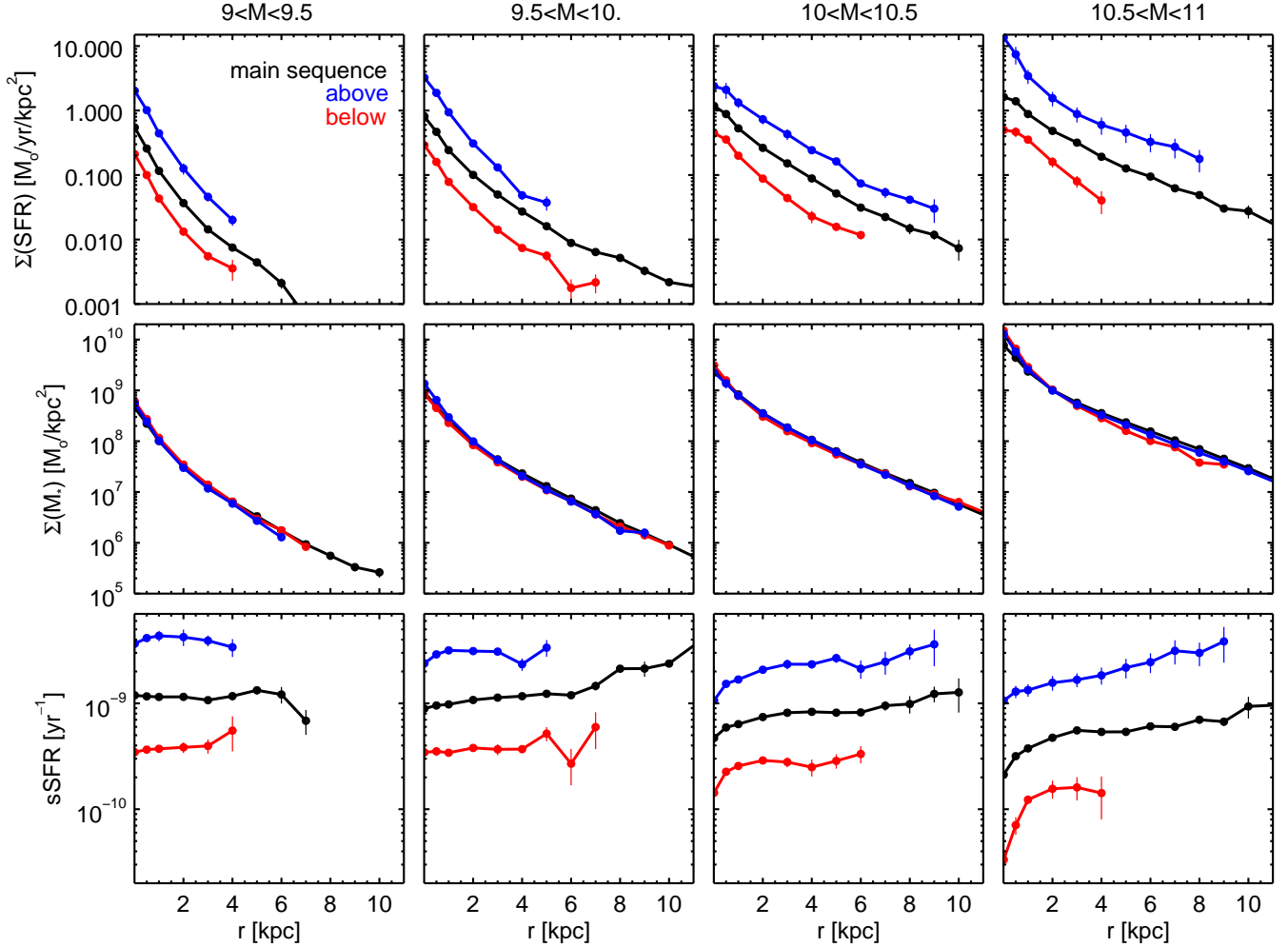
FIG. 13.— Radial surface brightness profiles of SFR, M∗, and their ratio sSFR as a function of M∗ and SFR. The colors delineate position with respect to the star forming 'main sequence': above (blue), on (black), and below (red). SFR and M∗ profiles are Hα and H_{F140W} profiles scaled to the total SFR(UV+IR) and M∗ with all the caveats described in §8.1. Out to distances as great as 8 kpc from the galactic center, star formation is enhanced in galaxies above and depressed in galaxies below the star forming main sequence. This is also true of the specific star formation rate. In general, the radial distribution of M∗ is similar on, above, and below the main sequence on average. It becomes slightly more centrally concentrated in galaxies above and below the main sequence at the highest masses, as shown in Fig. 14. There are two take home messages from this figure: 1. The star formation rate, on average, is always the highest in the centers of galaxies. 2. The radial distribution of star formation depends more strongly on M∗ than SFR at fixed mass (a galaxy's position with respect to the main sequence).

fainter below but the underlying mass profiles are fairly similar at all SFRs (although see next section for a discussion of the highest masses). On the other hand, the dust attenuation increases with increasing SFR at fixed mass. Acting in concert, dust and age mean that the EW(Hα) profiles shown in the bottom panels of Fig. 9 likely underestimate the true difference in sSFR above, on, and below the main sequence. In the bottom panels of Fig. 13 the trends in sSFR are enhanced after accounting for dust and age.

The most robust conclusion we can draw about the radial distribution of star formation, an inferred quantity, is that star formation in the disk between 2 − 6 kpc is enhanced above the main sequence and suppressed below the main sequence. This, in turn, has several important implications.

First, our results constrain the importance of AGN emission above the main sequence. One possibility is that galaxies above the star forming main sequence are there because the bright UV+IR emission of an AGN was incorrectly interpreted as star formation. In this case, the Hα emission would

be elevated in the center but the same as on the main sequence throughout the rest of the disk. This, however, is not what we observe: the Hα in the disk from 2-6 kpc is elevated, meaning that galaxies are not only above the main sequence due to misinterpreted AGN.

Second, because Hα is an independent indicator of star formation, the fact that it is enhanced at all radii confirms that the scatter in the main sequence is real and due to variations in the star formation rate at fixed mass. If the observed main sequence scatter were due exclusively to measurement errors in the UV+IR SFRs, the Hα should not be enhanced or depressed in concert, but it is.

Third, the profiles provide information on the importance of mergers and galaxy encounters "pushing" galaxies above the main sequence. It is well established that interaction-driven gravitational torques can funnel gas to the center of a galaxy inducing a burst of star formation (e.g., Hernquist 1989; Barnes & Hernquist 1991, 1996; Mihos & Hernquist 1996). However, in idealized merger simulations, Moreno

et al. (2015) show that while star formation is enhanced in the central kpc of interacting galaxies, it is *suppressed* everywhere else. This is not what we observe: the Hα in our stacks above the main sequence is enhanced at all radii; it is not enhanced in the central kpc and suppressed at larger galacto-centric radii. Some ambiguity is inherent in the interpretation of an average distribution of Hα because the distribution of Hα in individual galaxies could vary significantly from the average. Our stacking method cannot distinguish between local enhancements at random locations in the disk and global enhancement of the disks of individual galaxies. Nevertheless, our uniformly higher star formation rates suggest that major mergers are not the *only* physical process driving the elevated star formation in galaxies above the star forming main sequence.

Below the main sequence, it is possible the dominant processes suppressing star formation act primarily in the centers of galaxies where AGN live, bulges grow, and timescales are short. If this were the case, we would expect Hα to be lower in the center of the galaxies but unchanged at large radii. Again, this is not what we observe: below the main sequence Hα is suppressed at all radii, indicating that the physical mechanisms suppressing star formation must act over the whole disk, not exclusively the center.

Instead perhaps, for stellar masses below $M \sim 3 \times 10^{10} M_\odot$, some cosmological hydrodynamic simulations (Sparre et al. 2015) and models (Dutton, van den Bosch, & Dekel 2010; Kelson 2014) have suggested that a galaxy's position in the SFR-M_* plane is driven by its mass accretion history. In this schema, galaxies living below the main sequence had early formation histories and galaxies above the main sequence had later formation histories. Sparre et al. (2015) show that in Illustris, most of the scatter in the star-forming main sequence is driven by these long scale ($\gtrsim 500$Myr) features of galaxies' formation trajectories rather than short-term stochasticity. Dutton et al. (2010) predict based on this model for main sequence scatter that the size of gas disks should be the same above and below the main sequence. Consistent with this prediction, for masses below $M \sim 10^{10.5} M_\odot$, we do not see significant differences in Hα sizes above and below the main sequence, although the error bars are large (see Table 2 for values). The fact that the average radial distribution of Hα does not have wildly different structure above and below the main sequence perhaps makes more sense in the context of scatter driven by longer timescale variations in the mass accretion history as opposed to some ubiquitous physical process. In other words, the similarity of the radial profiles appears consistent with a simple model in which the overall star formation rate scales with the gas accretion rate (averaged over some timescale) and the gas distributes itself in similar structures regardless of its accretion rate. It will be interesting to compare the observed gas distributions directly to those in galaxy formation models.

Regardless of the physical reasons, across the SFR-M_* plane two important features are consistent. 1) The observed Hα distribution is always centrally peaked. 2) The observed EW(Hα) is never centrally peaked.

7.5. *Bulge growth and quenching at high masses?*

While Hα is enhanced at all radii in galaxies above the main sequence and suppressed at all radii below the main sequence, in the high mass bin ($M = 10^{10.5} - 10^{11} M_\odot$), the trends appear to have some radial dependence as well. To examine trends

at high masses in more detail, in Fig. 14 we show the same the radial profiles of Hα, H_{F140W}, and EW(Hα) above, on and below the main sequence as in Figs. 9 and 13. Here we also normalize by the main sequence profiles to highlight differences.

Above the main sequence, there is a central excess in Hα emission (left panels of Fig. 14). The cause of this excess is difficult to interpret: it could be due to an AGN or extra star formation in the central regions or both. As mentioned in § 2.3, galaxies with X-ray luminosity $L_x > 10^{42.5}$erg s^{-1} or a very obvious broad line component are excluded from the analysis in this paper. The excess central Hα emission exists even when galaxies hosting obvious AGN are excluded. However, with a very conservative cut on broad line AGN in which galaxies with even marginal elongation in the spectral direction are excluded, the central excess in Hα disappears. Hence, it is possible that this central enhancement is driven primarily by emission from AGN. If it is due to an AGN, it could suggest that supermassive black holes are growing in this region of parameter space. If it is due to star formation, it could indicate that bulge construction is underway, consistent with the growing prominence of bulges observed during this epoch (Lang et al. 2014). We note that because the IR/Hα in this bin is so high, it is likely that the excess in central ionizing flux (either from star formation or an AGN) would actually be even larger if it were not attenuated.

If the high SFRs in galaxies above the main sequence are fueled by elevated gas accretion rates, the disks of these galaxies are likely to be gas-rich. In these gas-rich environments, it has been suggested that gravitational torques induced by violent disk instability could drive gas rapidly inward by viscous and dynamical friction (Noguchi 1999; Dekel, Sari, & Ceverino 2009a; Krumholz & Burkert 2010; Bournaud et al. 2011; Genzel et al. 2011; Forbes, Krumholz, & Burkert 2012; Cacciato, Dekel, & Genel 2012; Elmegreen, Zhang, & Hunter 2012; Dekel et al. 2013; Forbes et al. 2014). Once in the center this gas could fuel the bulge and/or black hole growth evidenced by the excess central Hα emission.

During the epoch $0.7 < z < 1.5$ in this mass range ($M = 10^{10.5} - 10^{11} M_\odot$) the quenched fraction roughly doubles (from $\sim 30 - 60\%$). Since the SFRs of galaxies must fall below the main sequence on their way to quenchdom, this region of parameter space would be a good place to look for hints as to how galaxies quench. Relative to the main sequence, the Hα below the main sequence appears to be depressed in the center (Fig. 14 bottom left). The Hα profile also appears depressed relative to the main sequence at larger radii, a manifestation of its smaller scale radius (Fig. 15). That is, we find that below the main sequence, the star-forming disk of Hα emission is both less centrally concentrated and more compact.

In addition to the Hα in the centers of galaxies below the main sequence being depressed relative to galaxies on the main sequence, it is also depressed relative to the H_{F140W} emission (Fig. 14, top right). Interpreted as sSFR, this means that the stellar mass doubling time in the centers of these galaxies is significantly lower than at larger radii. Centrally depressed sSFR has been taken as evidence of inside-out quenching (Tacchella et al. 2015a). Here we show this for the first time explicitly below the main sequence where it is most straight-forward to interpret in the context of star formation quenching. That being said, it should be noted that although the Hα is centrally depressed in two interesting relative senses (relative to the H_{F140W} and relative to the main

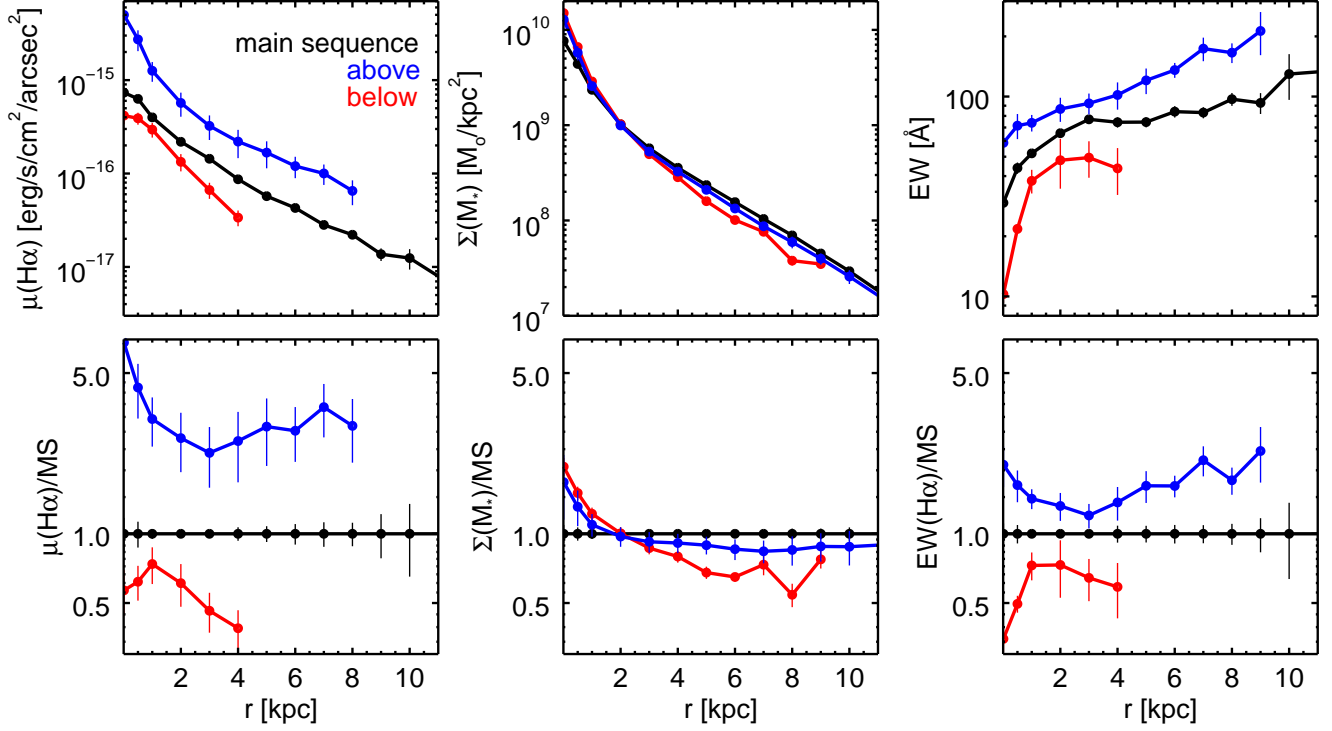FIG. 14.— Top row, radial profiles of Hα, M$_*$, and EW(Hα) for galaxies with M = $10^{10.5} - 10^{11} M_\odot$. As previously, the colors delineate position with respect to the star forming 'main sequence': above (blue), on (black), and below (red). The bottom row shows these profiles normalized by the main sequence (with the black line divided out). Above the main sequence, the Hα (and EW(Hα)) is enhanced at all radii, but somewhat more so at small and large radii. Below the main sequence, the Hα (and EW(Hα)) is suppressed at all radii, but somewhat more so small and large radii. There appears to be excess central stellar mass similarly above and below the main sequence.
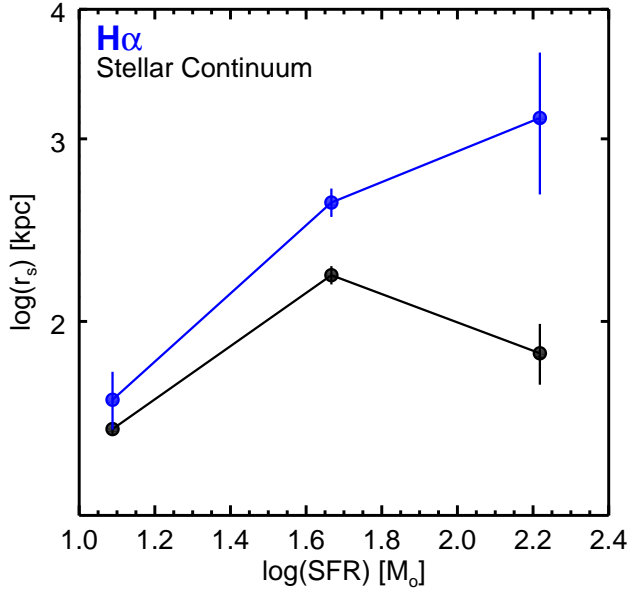

FIG. 15.— Relation between disk scale length and SFR in Hα and H_{F140W} emission for galaxies with $10.5 < \log(M_*) < 11.0$. In H_{F140W} emission, the disk scale length is smaller above and below the main sequence than on it. In Hα emission, the disk scale length below the main sequence remains smaller than on the main sequence but is larger above it.

sequence Hα), in an absolute sense, the Hα is *not* centrally depressed, it is centrally peaked. That is, on average, there is not a hole in the observed Hα emission at the centers of massive galaxies below the main sequence. So while we may be seeing some suppression of star formation in the center of these galaxies below the main sequence, it is not 'quenching' in the standard sense of a complete cessation of star formation.

Our findings could be viewed in the context of an evolutionary pathway from bulge growth to quenching (e.g., Wuyts et al. 2011a; Lang et al. 2014; Genzel et al. 2014b; Tacchella et al. 2015a). Consistent with Wuyts et al. (2011a), we find excess central stellar continuum emission similarly above and below the star forming sequence. Wuyts et al. (2011a) suggests that this structural similarity could indicate an evolutionary link between the galaxies above and below the main sequence.

AGN can in principle drive gas out of the centers of their host galaxies, efficiently removing the fuel for star formation (see e.g., Croton et al. 2006). Large bulges are also in principle capable of stabilizing galaxy disks and suppressing star formation from the inside-out ('gravitational quenching' Martig et al. 2009; Genzel et al. 2014b). Observationally, it seems that regardless the physical cause, galaxies quench after reaching a stellar surface density threshold (e.g. Franx et al. 2008). Whatever process is underway above the main sequence, there are theoretical indications that it is capable of suppressing star formation. Some authors argue this occurs from the inside-out. The deep depression in EW(Hα) in the

centers of galaxies below the main sequence could be taken as evidence for one of these quenching mechanisms acting in this way.

One remaining mystery, as shown in Fig. 15 is that the Hα disks have much smaller sizes below the main sequence than on or above it. It is possible that the galaxies below the main sequence formed earlier than the galaxies on or above the main sequence at this redshift and hence the galaxies above the main sequence are not actually direct progenitors of those below. It is also possible that these galaxies underwent some sort of compaction on their way to quenching (e.g. Dekel & Burkert 2014; Zolotov et al. 2015) The most robust thing we can say is that below the main sequence, Hα seems to be both less centrally concentrated and less extended. How exactly this should be interpreted is unclear without the aid of simulations.

7.6. *The average spatial distribution of star formation from* $z = 0.7 - 1.5$

In § 4 & 5 we determined the radial profiles of star formation as a function of M_* and SFR. Here we briefly analyze the radial distribution of all star formation at this epoch, that is, at what distance from the center of a galaxy is a star most likely to form. The average Hα image of all selected galaxies is shown in Fig. 16. This is the average spatial distribution of Hα in galaxies during the epoch $0.7 < z < 1.5$. Each galaxy has an Hα map with a depth of 2 orbits on HST. We summed the Hα maps of 2676 galaxies, creating the equivalent of a 5352 orbit Hα image. This average Hα image is deepest Hα image in existence for galaxies at this epoch. With this stacked 5352 orbit HST image, we can trace the radial distribution of Hα down to a surface brightness limit of $1 \times 10^{-18}\,\mathrm{erg\,s^{-1}\,cm^{-2}\,arcsec^{-2}}$. This allows us to map the distribution of Hα emission out to $\sim 14\,\mathrm{kpc}$ where the star formation surface density is $4 \times 10^{-4}\,\mathrm{M_\odot\,yr^{-1}\,kpc^{-2}}$ (Kennicutt 1998).

Weighting the radial profile of Hα by area shows its probability distribution. The Hα probability distribution has a peak, the expectation value, at 0.75 kpc. Note, we did not normalize by the H_{F140W} flux here so the expectation value reflects the most likely place for a random HII region within a galaxy to exist. If we interpret Hα as star formation then during the epoch $0.7 < z < 1.5$, when $\sim 33\%$ of the total star formation in the history of the universe occurred, the most likely place for a new star to be born was 0.75 kpc from the center of its home galaxy.

8. CONCLUSIONS

In this paper, we studied galaxy growth through star formation during the epoch $0.7 < z < 1.5$ through a new window provided by the WFC3 G141 grism on HST. This slitless grism spectroscopy from space, with its combination of high spatial resolution and low spectral resolution gives spatially resolved Hα information, for 2676 galaxies over a large swath of the SFR-M_* plane. Hα can be used as a proxy for star formation, although there are many uncertainties (§ 7.1). The most important new observational result of our study is the behavior of the Hα profiles above and below the main sequence: remarkably, star formation is enhanced at all radii above the main sequence, and suppressed at all radii below the main sequence (Fig. 13). This means that the scatter in the star forming sequence is real. It also suggests that the primary mode of star formation is similar across all regions of this parameter space.

Across the expanse of the SFR-M_* plane, the radial distribution of star formation can be characterized in the following way. Most of the star formation appears to occur in disks (Fig. 5), which are well-aligned with the stellar distribution (Fig. 11). To first order, Hα and stellar continuum emission trace each other quite well. On average, the Hα surface density is always highest in the centers of galaxies, just like the stellar mass surface density. On the other hand, the EW(Hα), and the inferred specific star formation rate, is, on average, *never* highest in the centers of galaxies (Fig. 9). Taken at face value, this means that star formation is slightly more extended than the existing stars (Fig. 6), demonstrating that galaxies at this epoch are growing in size due to star formation.

The results in this study can be extended in many ways. In principle, the same dataset can be used to study the spatial distribution of [O III] emission at higher redshifts, although it is more difficult to interpret and the fact that it is a doublet poses practical difficulties. With submm interferometers such as NOEMA and ALMA the effects of dust obscuration can be mapped. Although it will be difficult to match the resolution and sample size that we reach in this study, this is crucial as dust is the main uncertainty in the present analysis. Finally, joint studies of the evolution of the distribution of star formation and the stellar mass can provide constraints on the importance of mergers and stellar migration in the build-up of present-day disks.

REFERENCES

Abramson, L. E., Kelson, D. D., Dressler, A., et al. 2014, ApJ, 785, L36
Adelberger, K. L., & Steidel, C. C. 2000, ApJ, 544, 218
Agertz, O., Teyssier, R., & Moore, B. 2011, Monthly Notices of the Royal Astronomical Society: Letters, 410, 1391
Atek, H., Malkan, M., McCarthy, P., et al. 2010, ApJ, 723, 104
Aumer, M., White, S. D. M., Naab, T., & Scannapieco, C. 2013, MNRAS, 434, 3142
Barnes, J. E., & Hernquist, L. 1996, ApJ, 471, 115
Barnes, J. E., & Hernquist, L. E. 1991, ApJ, 370, L65
Behroozi, P. S., Marchesini, D., Wechsler, R. H., et al. 2013, ApJ, 777, L10
Bell, E. F., Papovich, C., Wolf, C., et al. 2005, ApJ, 625, 23
Boada, S., Tilvi, V., Papovich, C., et al. 2015, eprint arXiv:1503.00722, 1503.00722
Bournaud, F., Dekel, A., Teyssier, R., et al. 2011, ApJ, 741, L33
Brammer, G., Pirzkal, N., McCullough, P., & MacKenty, J. 2014, Time-varying Excess Earth-glow Backgrounds in the WFC3/IR Channel, Tech. rep.
Brammer, G. B., van Dokkum, P. G., & Coppi, P. 2008, ApJ, 686, 1503
Brammer, G. B., van Dokkum, P. G., Illingworth, G. D., et al. 2013, ApJ, 765, L2
Brammer, G. B., van Dokkum, P. G., Franx, M., et al. 2012a, ApJS, 200, 13
Brammer, G. B., Sánchez-Janssen, R., Labbé, I., et al. 2012b, ApJ, 758, L17

Brennan, R., Pandya, V., Somerville, R. S., et al. 2015, eprint arXiv:1501.06840, 1501.06840
Brinchmann, J., Charlot, S., White, S. D. M., et al. 2004, MNRAS, 351, 1151
Brooks, A. M., Governato, F., Quinn, T., Brook, C. B., & Wadsley, J. 2009, The Astrophysical Journal, 694, 396
Brooks, A. M., Solomon, A. R., Governato, F., et al. 2011, ApJ, 728, 51
Bruce, V. A., Dunlop, J. S., McLure, R. J., et al. 2014, Monthly Notices of the Royal Astronomical Society: Letters, 444, 1660
Bruzual, G., & Charlot, S. 2003, Monthly Notices of the Royal Astronomical Society, 344, 1000
Buitrago, F., Trujillo, I., Conselice, C. J., et al. 2008, The Astrophysical Journal, 687, L61
Cacciato, M., Dekel, A., & Genel, S. 2012, MNRAS, 421, 818
Calzetti, D., Armus, L., Bohlin, R. C., et al. 2000, ApJ, 533, 682
Calzetti, D., Kinney, A. L., & Storchi-Bergmann, T. 1994, ApJ, 429, 582
Chabrier, G. 2003, PASP, 115, 763
Charlot, S., & Fall, S. M. 2000, ApJ, 539, 718
Contini, T., Garilli, B., Le Fèvre, O., et al. 2012, A&A, 539, A91
Croton, D. J., Springel, V., White, S. D. M., et al. 2006, MNRAS, 365, 11
Daddi, E., Dickinson, M., Morrison, G., et al. 2007, ApJ, 670, 156
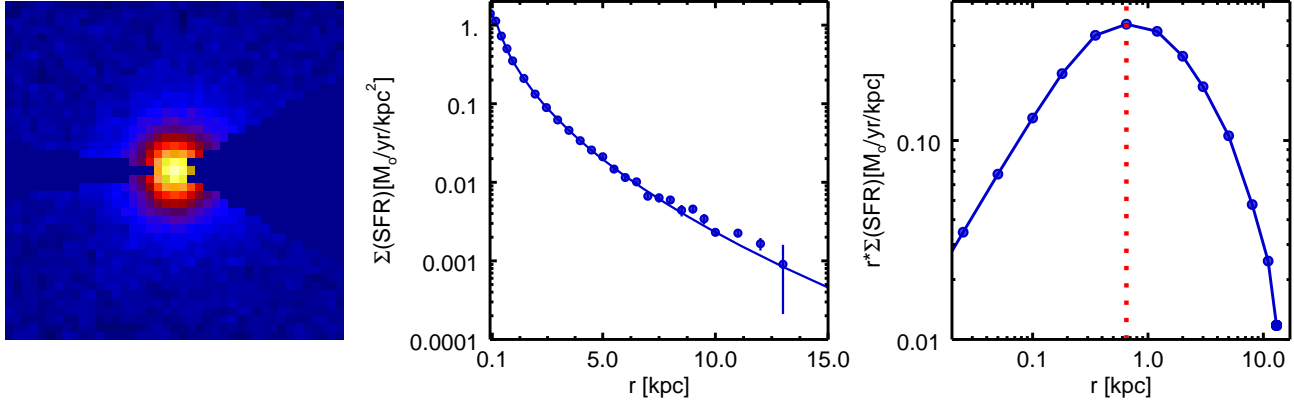Dalcanton, J. J., Spergel, D. N., & Summers, F. J. 1997, The Astrophysical Journal, 482, 659

FIG. 16.— Stack of all Hα for the redshift epoch $0.7 < z < 1.5$ and the corresponding average radial distribution (left and center.) Weighting by area shows where the average star formed during this epoch: ~ 0.75 kpc from the center of it's home galaxy.

Dale, D. A., & Helou, G. 2002, The Astrophysical Journal, 576, 159
Damen, M., Labbé, I., Franx, M., et al. 2009, ApJ, 690, 937
Dekel, A., & Birnboim, Y. 2006, Monthly Notices of the Royal Astronomical Society: Letters, 368, 2
Dekel, A., & Burkert, A. 2014, MNRAS, 438, 1870
Dekel, A., Sari, R., & Ceverino, D. 2009a, ApJ, 703, 785
Dekel, A., Zolotov, A., Tweed, D., et al. 2013, MNRAS, 435, 999
Dekel, A., Birnboim, Y., Engel, G., et al. 2009b, Nature, 457, 451
Domínguez, A., Siana, B., Henry, A. L., et al. 2013, ApJ, 763, 145
Dutton, A. A., & van den Bosch, F. C. 2012, MNRAS, 421, 608
Dutton, A. A., van den Bosch, F. C., & Dekel, A. 2010, MNRAS, 405, 1690
Elbaz, D., Daddi, E., Le Borgne, D., et al. 2007, A&A, 468, 33
Elmegreen, B. G., Zhang, H.-X., & Hunter, D. A. 2012, ApJ, 747, 105
Epinat, B., Contini, T., Le Fèvre, O., et al. 2009, Astronomy and Astrophysics, 504, 789
Epinat, B., Tasca, L., Amram, P., et al. 2012, A&A, 539, A92
Erb, D. K., Steidel, C. C., Shapley, A. E., et al. 2006a, ApJ, 647, 128
—. 2006b, ApJ, 646, 107
Fall, S. M., & Efstathiou, G. 1980, MNRAS, 193, 189
Ferguson, H. C., Dickinson, M., Giavalisco, M., et al. 2004, The Astrophysical Journal, 600, L107
Forbes, J., Krumholz, M., & Burkert, A. 2012, ApJ, 754, 48
Forbes, J. C., Krumholz, M. R., Burkert, A., & Dekel, A. 2014, MNRAS, 438, 1552
Förster Schreiber, N. M., Shapley, A. E., Erb, D. K., et al. 2011a, ApJ, 731, 65
Förster Schreiber, N. M., Genzel, R., Lehnert, M. D., et al. 2006, ApJ, 645, 1062
Förster Schreiber, N. M., Genzel, R., Bouché, N., et al. 2009, ApJ, 706, 1364
Förster Schreiber, N. M., Shapley, A. E., Genzel, R., et al. 2011b, ApJ, 739, 45
Förster Schreiber, N. M., Genzel, R., Newman, S. F., et al. 2014, The Astrophysical Journal, 787, 38
Franx, M., van Dokkum, P. G., Schreiber, N. M. F., et al. 2008, ApJ, 688, 770
Fumagalli, M., Patel, S. G., Franx, M., et al. 2012, eprint arXiv:1206.1867, 757, L22
Geach, J. E., Smail, I., Best, P. N., et al. 2008, MNRAS, 388, 1473
Genel, S., Fall, S. M., Hernquist, L., et al. 2015, ArXiv e-prints, arXiv:1503.01117
Genzel, R., Burkert, A., Bouché, N., et al. 2008, ApJ, 687, 59
Genzel, R., Newman, S., Jones, T., et al. 2011, ApJ, 733, 101
Genzel, R., Förster Schreiber, N. M., Rosario, D., et al. 2014a, ApJ, 796, 7
Genzel, R., Förster Schreiber, N. M., Lang, P., et al. 2014b, ApJ, 785, 75
Giavalisco, M., Steidel, C. C., & Macchetto, F. D. 1996, The Astrophysical Journal, 470, 189
González, V., Labbé, I., Bouwens, R. J., et al. 2010, ApJ, 713, 115
Governato, F., Brook, C., Mayer, L., et al. 2010, Nature, 463, 203
Grogin, N. A., Kocevski, D. D., Faber, S. M., et al. 2011, ApJS, 197, 35
Guedes, J., Callegari, S., Madau, P., & Mayer, L. 2011, The Astrophysical Journal, 742, 76
Hernquist, L. 1989, Nature, 340, 687
Hopkins, A. M., Connolly, A. J., Haarsma, D. B., & Cram, L. E. 2001, AJ, 122, 288
Huang, S., Haynes, M. P., Giovanelli, R., & Brinchmann, J. 2012, ApJ, 756, 113
Hummels, C. B., & Bryan, G. L. 2012, ApJ, 749, 140
Jones, T., Ellis, R. S., Richard, J., & Jullo, E. 2013, ApJ, 765, 48
Jones, T., Wang, X., Schmidt, K. B., et al. 2015, AJ, 149, 107
Karim, A., Schinnerer, E., Martínez-Sansigre, A., et al. 2011, The Astrophysical Journal, 730, 61
Kashino, D., Silverman, J. D., Rodighiero, G., et al. 2013, ApJ, 777, L8
Kelson, D. D. 2014, ArXiv e-prints, arXiv:1406.5191

Kennicutt, Jr., R. C. 1998, ApJ, 498, 541
Keres, D., Katz, N., Fardal, M., Davé, R., & Weinberg, D. H. 2009, Monthly Notices of the Royal Astronomical Society: Letters, 395, 160
Keres, D., Katz, N., Weinberg, D. H., & Davé, R. 2005, Monthly Notices of the Royal Astronomical Society: Letters, 363, 2
Koekemoer, A. M., Faber, S. M., Ferguson, H. C., et al. 2011, ApJS, 197, 36
Kornei, K. A., Shapley, A. E., Martin, C. L., et al. 2012, ApJ, 758, 135
Kriek, M., van Dokkum, P. G., Franx, M., Illingworth, G. D., & Magee, D. K. 2009, ApJ, 705, L71
Kriek, M., Shapley, A. E., Reddy, N. A., Siana, B. 2015, ApJS, 218, 15
Krist, J. 1995, in Astronomical Society of the Pacific Conference Series, Vol. 77, Astronomical Data Analysis Software and Systems IV, ed. R. A. Shaw, H. E. Payne, & J. J. E. Hayes, 349
Krumholz, M., & Burkert, A. 2010, ApJ, 724, 895
Labbe, I., Huang, J., Franx, M., et al. 2005, The Astrophysical Journal, 624, L81
Lang, P., Wuyts, S., Somerville, R. S., et al. 2014, ApJ, 788, 11
Leja, J., van Dokkum, P. G., Franx, M., & Whitaker, K. E. 2015, ApJ, 798, 115
Leja, J., van Dokkum, P. G., Momcheva, I., et al. 2013, ApJ, 778, L24
Lu, Z., Mo, H. J., Lu, Y., et al. 2014, MNRAS, 439, 1294
Magdis, G. E., Rigopoulou, D., Huang, J.-S., & Fazio, G. G. 2010, MNRAS, 401, 1521
Maiolino, R., Nagao, T., Grazian, A., et al. 2008, A&A, 488, 463
Mancini, C., Förster Schreiber, N. M., Renzini, A., et al. 2011, The Astrophysical Journal, 743, 86
Marinacci, F., Pakmor, R., & Springel, V. 2013, eprint arXiv:1305.5360
Marsan, Z. C., Marchesini, D., Brammer, G. B., et al. 2015, ApJ, 801, 133
Martig, M., Bournaud, F., Teyssier, R., & Dekel, A. 2009, ApJ, 707, 250
Mihos, J. C., & Hernquist, L. 1996, ApJ, 464, 641
Mo, H. J., Mao, S., & White, S. D. M. 1998, Monthly Notices of the Royal Astronomical Society, 295, 319
Momcheva, I. G., Lee, J. C., Ly, C., et al. 2013, AJ, 145, 47
Moreno, J., Torrey, P., Ellison, S. L., et al. 2015, MNRAS, 448, 1107
Mosleh, M., Williams, R. J., Franx, M., et al. 2012, The Astrophysical Journal, 756, L12
Moster, B. P., Naab, T., & White, S. D. M. 2013, MNRAS, 428, 3121
Muzzin, A., van Dokkum, P., Kriek, M., et al. 2010, ApJ, 725, 742
Nelson, D., Genel, S., Vogelsberger, M., et al. 2015, MNRAS, 448, 59
Nelson, E., van Dokkum, P., Franx, M., et al. 2014, Nature, 513, 394
Nelson, E. J., van Dokkum, P. G., Brammer, G., et al. 2012, ApJ, 747, L28
Nelson, E. J., van Dokkum, P. G., Momcheva, I., et al. 2013, The Astrophysical Journal, 763, L16
Newman, S. F., Genzel, R., Förster-Schreiber, N. M., et al. 2012, ApJ, 761, 43
Noeske, K. G., Weiner, B. J., Faber, S. M., et al. 2007, ApJ, 660, L43
Noguchi, M. 1999, ApJ, 514, 77
Oesch, P. A., Bouwens, R. J., Carollo, C. M., et al. 2010, The Astrophysical Journal, 709, L21
Pannella, M., Carilli, C. L., Daddi, E., et al. 2009, ApJ, 698, L116
Papovich, C., Labbé, I., Quadri, R., et al. 2015, The Astrophysical Journal, 803, 26
Patel, S. G., van Dokkum, P. G., Franx, M., et al. 2013, The Astrophysical Journal, 766, 15
Peng, C. Y., Ho, L. C., Impey, C. D., & Rix, H.-W. 2002, AJ, 124, 266
Peth, M. A., Lotz, J. M., Freeman, P. E., et al. 2015, eprint arXiv:1504.01751, 1504.01751
Price, S. H., Kriek, M., Brammer, G. B., et al. 2014, ApJ, 788, 86
Queyrel, J., Contini, T., Kissler-Patig, M., et al. 2012, A&A, 539, A93
Reddy, N. A., Erb, D. K., Pettini, M., Steidel, C. C., & Shapley, A. E. 2010, ApJ, 712, 1070
Reddy, N. A., Steidel, C. C., Fadda, D., et al. 2006, ApJ, 644, 792

Reddy, N. A., Kriek, M., Shapley, A. E., et al. 2015, ArXiv e-prints, arXiv:1504.02782
Rosario, D. J., Santini, P., Lutz, D., et al. 2013, ApJ, 771, 63
Roškar, R., Debattista, V. P., Stinson, G. S., et al. 2008, The Astrophysical Journal, 675, L65
Sales, L. V., Navarro, J. F., Schaye, J., et al. 2010, MNRAS, 409, 1541
Sales, L. V., Navarro, J. F., Theuns, T., et al. 2012, MNRAS, 423, 1544
Salim, S., Rich, R. M., Charlot, S., et al. 2007, UV Star Formation Rates in the Local Universe, arXiv:0704.3611
Sanders, R. L., Shapley, A. E., Kriek, M., et al. 2015, The Astrophysical Journal, 799, 138
Savaglio, S., Glazebrook, K., Le Borgne, D., et al. 2005, ApJ, 635, 260
Scannapieco, C., Wadepuhl, M., Parry, O. H., et al. 2012, Monthly Notices of the Royal Astronomical Society: Letters, 423, 1726
Shapiro, K. L., Genzel, R., Quataert, E., et al. 2009, ApJ, 701, 955
Shapley, A. E., Steidel, C. C., Pettini, M., & Adelberger, K. L. 2003, ApJ, 588, 65
Shapley, A. E., Reddy, N. A., Kriek, M., et al. 2015, The Astrophysical Journal, 801, 88
Shen, S., Mo, H. J., White, S. D. M., et al. 2003, MNRAS, 343, 978
Simpson, J. M., Smail, I., Swinbank, A. M., et al. 2015, ApJ, 799, 81
Skelton, R. E., Whitaker, K. E., Momcheva, I. G., et al. 2014, ArXiv e-prints, arXiv:1403.3689
Sobral, D., Best, P. N., Matsuda, Y., et al. 2012, MNRAS, 420, 1926
Sobral, D., Best, P. N., Geach, J. E., et al. 2009, MNRAS, 398, 75
Sparre, M., Hayward, C. C., Springel, V., et al. 2015, MNRAS, 447, 3548
Stinson, G. S., Bovy, J., Rix, H.-W., et al. 2013, MNRAS, 436, 625
Stott, J. P., Sobral, D., Swinbank, A. M., et al. 2014, MNRAS, 443, 2695
Swinbank, M., Smail, I., Sobral, D., et al. 2012, eprint arXiv:1206.1867
Szomoru, D., Franx, M., van Dokkum, P. G., et al. 2013, ApJ, 763, 73
Tacchella, S., Carollo, C. M., Renzini, A., et al. 2015a, Science, 348, 314
Tacchella, S., Lang, P., Carollo, C. M., et al. 2015b, ApJ, 802, 101
Toft, S., van Dokkum, P., Franx, M., et al. 2007, ApJ, 671, 285
Trujillo, I., Forster Schreiber, N. M., Rudnick, G., et al. 2006, The Astrophysical Journal, 650, 18
Übler, H., Naab, T., Oser, L., et al. 2014, MNRAS, 443, 2092
van den Bosch, F. C. 2001, Monthly Notices of the Royal Astronomical Society, 327, 1334

van der Wel, A., Bell, E. F., Häussler, B., et al. 2012, ApJS, 203, 24
van der Wel, A., Franx, M., van Dokkum, P. G., et al. 2014a, The Astrophysical Journal, 788, 28
van der Wel, A., Chang, Y.-Y., Bell, E. F., et al. 2014b, The Astrophysical Journal, 792, L6
van Dokkum, P. G., Franx, M., Fabricant, D., Illingworth, G. D., & Kelson, D. D. 2000, ApJ, 541, 95
van Dokkum, P. G., Whitaker, K. E., Brammer, G., et al. 2010, ApJ, 709, 1018
van Dokkum, P. G., Brammer, G., Fumagalli, M., et al. 2011, ApJ, 743, L15
van Dokkum, P. G., Leja, J., Nelson, E. J., et al. 2013, The Astrophysical Journal, 771, L35
van Dokkum, P. G., Nelson, E. J., Franx, M., et al. 2015, ArXiv e-prints, arXiv:1506.03085
Wang, B., & Heckman, T. M. 1996, ApJ, 457, 645
Whitaker, K. E., van Dokkum, P. G., Brammer, G., & Franx, M. 2012, ApJ, 754, L29
Whitaker, K. E., Labbé, I., van Dokkum, P. G., et al. 2011, ApJ, 735, 86
Whitaker, K. E., Franx, M., Leja, J., et al. 2014, ApJ, 795, 104
White, S. D. M., & Rees, M. J. 1978, Monthly Notices of the Royal Astronomical Society: Letters, 183, 341
Williams, R. J., Quadri, R. F., Franx, M., et al. 2010, ApJ, 713, 738
Wisnioski, E., Förster Schreiber, N. M., Wuyts, S., et al. 2015, ApJ, 799, 209
Wuyts, E., Kurk, J., Förster Schreiber, N. M., et al. 2014, ApJ, 789, L40
Wuyts, S., Labbé, I., Schreiber, N. M. F., et al. 2008, ApJ, 682, 985
Wuyts, S., Labbé, I., Franx, M., et al. 2007, ApJ, 655, 51
Wuyts, S., Förster Schreiber, N. M., van der Wel, A., et al. 2011a, ApJ, 742, 96
Wuyts, S., Förster Schreiber, N. M., Lutz, D., et al. 2011b, ApJ, 738, 106
Wuyts, S., Förster Schreiber, N. M., Genzel, R., et al. 2012, ApJ, 753, 114
Wuyts, S., Förster Schreiber, N. M., Nelson, E. J., et al. 2013, ApJ, 779, 135
Yang, X., Mo, H. J., van den Bosch, F. C., Zhang, Y., & Han, J. 2012, ApJ, 752, 41
Yoshikawa, T., Akiyama, M., Kajisawa, M., et al. 2010, ApJ, 718, 112
Yuan, T.-T., Kewley, L. J., Swinbank, A. M., Richard, J., & Livermore, R. C. 2011, ApJ, 732, L14
Zahid, H. J., Geller, M. J., Kewley, L. J., et al. 2013, ApJ, 771, L19
Zheng, X. Z., Bell, E. F., Papovich, C., et al. 2007, ApJ, 661, L41
Zolotov, A., Dekel, A., Mandelker, N., et al. 2015, MNRAS, 450, 2327

9. APPENDIX

In this paper we investigate the average radial distribution of Hα emission by stacking the Hα maps of individual galaxies and computing the flux in circular apertures on this stack. With this methodology, we average over the distribution of inclination angles, position angles, and sizes of galaxies that go into each stack. The simplicity of this method has a number of advantages. First, it requires no assumptions about the intrinsic properties of galaxies. Second, it allows us to measure the average size of the Hα distribution in the star forming disk. Finally, because the image plane is left in tact, we can correct for the PSF.

To complement this analysis, here we present the average deprojected, radially-normalized distribution of Hα. We do this to test the effect of projection and a heterogenous mix of sizes on the shape of the radial profile of Hα, to ensure trends were not washed out with the simpler methodology employed in the rest of the paper.

To do this, we use GALFIT (Peng et al. 2002) to derive the effective radius, axis ratio, and position angle of each galaxy from its H_{F140W} stellar continuum image. We correct for the inclination angle of each galaxy by deprojecting the (x,y) pixel grid of it's image based on the inclination angle implied by the axis ratio. The surface brightness profile is computed by measuring the flux in deprojected radial apertures. In practice, this is done simply by extracting the radial profile of each galaxy in elliptical apertures defined by the position angle, axis ratio, and center of the H_{F140W} image. The extraction apertures were normalized by the H_{F140W} effective radius of each galaxy. A radial profile in deprojected, r_e-normalized space is derived for each galaxy. These individual galaxy profiles are flux-normalized by their integrated H_{F140W} magnitude and summed to derive the mean radial distribution.

The average de-projected, r_e-normalized radial profiles of Hα, H_{F140W}, and EW(Hα) are shown in Fig. 17. In general, the qualitative trends seen here are the same as those described in the main text. For the region $0.5 < r_e < 3$ the radial profile of Hα remains consistent with an exponential all masses, above, on, and below the star forming sequence. The radial profiles of both Hα and H_{F140W} are somewhat less centrally peaked than the analogous profiles in Fig. 9. This is expected of disk-dominated galaxies under different orientation angles as flux from the disk of edge-on galaxies could be projected onto the center. Additionally, stacking galaxies of different sizes can result in a somewhat steeper (higher n) profile than the individual galaxies that went into it (see van Dokkum et al. 2010). Because the shapes of the Hα and H_{F140W} profiles are similarly effected by deriving the profiles with this different methodology, the shape of the EW(Hα) profiles remain largely unchanged.
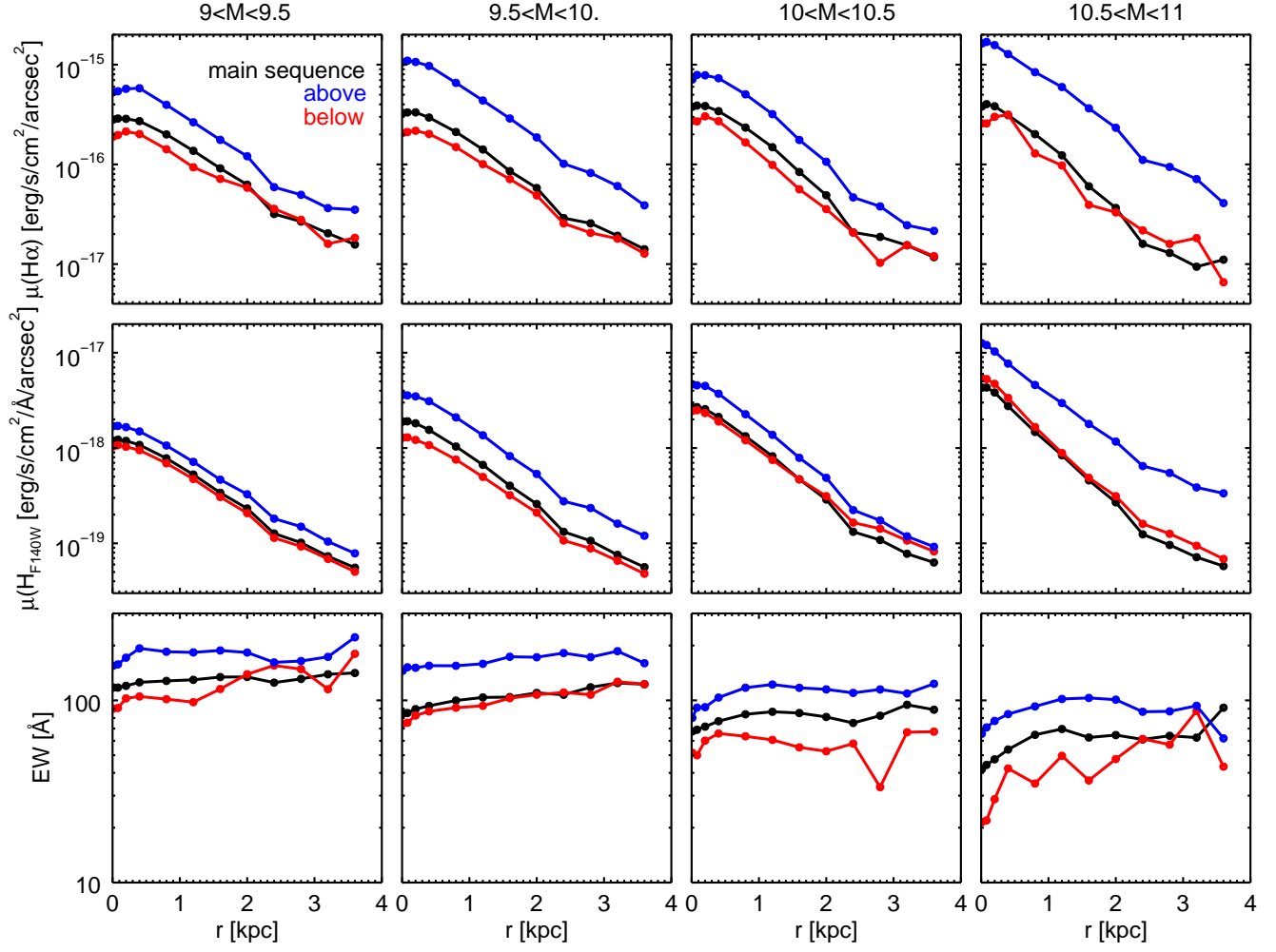
FIG. 17.— Average de-projected, r_e-normalized radial profiles of Hα, H_{F140W}, and EW(Hα) as a function of mass.